AFOSR-TR- 78 - 1402

LEVEL II

IMS

INSTITUTE OF MATERIALS SCIENCE

AD A060362

D D C

RECEIVED

OCT 26 1978

D

THE UNIVERSITY OF CONNECTICUT
Storrs · Connecticut

78 10 16 115

LEVEL II

Interim Scientific Report
to
United States Air Force
Air Force Office of Scientific Research
Wear of Homogeneous and Composite Materials Under
Conditions of Repeated Normal and Sliding Impact

AFOSR - 76 - 3087

D D C

RECEIVED
OCT 26 1978
D

78 10 16 115

LEVEL

REPORT DOCUMENTATION PAGE		READ INSTRUCTIONS BEFORE COMPLETING FORM
1. REPORT NUMBER AFOSR-TR- 78-1402	2. GOVT ACCESSION NO.	3. RECIPIENT'S CATALOG NUMBER
4. TITLE *(and Subtitle)* WEAR OF HOMOGENEOUS AND COMPOSITE MATERIALS UNDER CONDITIONS OF REPEATED NORMAL AND SLIDING IMPACT.		5. TYPE OF REPORT & PERIOD COVERED INTERIM scientific rept. 8 July 1977 - 7 July 1978
		6. PERFORMING ORG. REPORT NUMBER
7. AUTHOR(s) STEPHEN L. RICE ROMAN SOLECKI		8. CONTRACT OR GRANT NUMBER(s) AFOSR 76 -3087
9. PERFORMING ORGANIZATION NAME AND ADDRESS THE UNIVERSITY OF CONNECTICUT INSTITUTE OF MATERIALS SCIENCES STORRS, CONNECTICUT, 06268		10. PROGRAM ELEMENT, PROJECT, TASK AREA & WORK UNIT NUMBERS 2307 B2 26110F
11. CONTROLLING OFFICE NAME AND ADDRESS AIR FORCE OFFICE OF SCIENTIFIC RESEARCH/NA BLDG 410 BOLLING AIR FORCE BASE, D C 20332		12. REPORT DATE 1978
		13. NUMBER OF PAGES 64
14. MONITORING AGENCY NAME & ADDRESS *(if different from Controlling Office)*		15. SECURITY CLASS. *(of this report)* UNCLASSIFIED
		15a. DECLASSIFICATION/DOWNGRADING SCHEDULE

16. DISTRIBUTION STATEMENT *(of this Report)*

Approved for public release; distribution unlimited.

17. DISTRIBUTION STATEMENT *(of the abstract entered in Block 20, if different from Report)*

18. SUPPLEMENTARY NOTES

19. KEY WORDS *(Continue on reverse side if necessary and identify by block number)*

WEAR   WEIGHT LOSS
SLIDING   MICROSTRUCTURE
IMPACT
TRIBOLOGY
MATERIALS

20. ABSTRACT *(Continue on reverse side if necessary and identify by block number)*

This report describes experimental and analytical investigations in the area of wear of materials due to repeated impact loading. A reciprocating impact wear test apparatus is utilized to provide controlled, repetitive impacts between a material specimen and a counterface. The impulsive loading may be purely normal or a condition of relative sliding may be introduced during the impact event. A wide variety of materials have been investigated in both normal and alising impact modes. These include polymers, composites, and several materials. The wear behavior of these materials is investigated as a function of peak impulsive

DD FORM
1 JAN 73   1473   EDITION OF 1 NOV 65 IS OBSOLETE

406 916

load, relative sliding velocity, and number of impact load cycles. Weight loss and/or surface profile data are obtained as a function of these parameters. Scanning electron microscope studies of the wear surface and of sub-surface sections suggest that delamination is the operative mechanism for some materials but not for others. Analytical investigations are directed toward determination of the states of stress in material specimens undergoing controlled, repetitive impact. Results are derived from the theory of elasticity by application of the Papkovich-Neuber solution combined with the double, finite Fourier transformation. Correlations between sub-surface stress levels and wear debris formation are sought.

Abstract

This report describes experimental and analytical investigations in the area of wear of materials due to repeated impact loading. A reciprocating impact wear test apparatus is utilized to provide controlled, repetitive impacts between a material specimen and a counterface. The impulsive loading may be purely normal or a condition of relative sliding may be introduced during the impact event. A wide variety of materials have been investigated in both normal and sliding impact modes. These include polymers, composites, and several metals. The wear behavior of these materials is investigated as a function of peak impulsive load, relative sliding velocity, and number of impact load cycles. Weight loss and/or surface profile data are obtained as a function of these parameters. Scanning electron microscope studies of the wear surface and of sub-surface sections suggest that delamination is the operative mechanism for some materials but not for others.

Analytical investigations are directed toward determination of the states of stress in material specimens undergoing controlled, repetitive impact. Results are derived from the theory of elasticity by application of the Papkovich-Neuber solution combined with the double, finite Fourier transformation. Correlations between sub-surface stress levels and wear debris formation are sought.

Experimental

As noted earlier [1], we have studied a broad range of materials of technological significance. These include polymers, composites, steels, and titanium and aluminum alloys. The following sections will summarize salient experimental results for each category of material noted above. A later section will summarize results which overlap the material domains.

A. Polymers

The polymeric materials tested were Teflon and Delrin (polytetra-fluoroethylene and acetal resin). Results from these test series have been reported [2]. It was found that wear laminae were particularly apparent in compound impact, where relative transverse sliding accompanies the normal impulse. Increased relative sliding speed was found to accelerate the process of surface and subsurface crack initiation, with increasing numbers of impact cycles tending to refine microcrack patterns.

The relatively amorphous nature of teflon as contrasted to the relatively crystalline structure of delrin gave rise to some concern over the mechanism of crack initiation in teflon. Based upon observations of microvoids in commercially produced polymeric materials [3,4], a mechanism for crack initiation in relatively amorphous polymers was postulated.

B. Composites

The graphite epoxy composites tested were machined from a press cured composite panel supplied from 3M Company and from pultruded rod furnished by Hercules, Inc. Preliminary results on the 3M product have been reported [5], and further work with both composites supports the earlier findings.

With fiber orientation parallel to the normal impact direction, both composites are found to possess excellent wear resistance. In particular, for compound impact loading where wear rates are normally appreciable for metallic and polymeric materials, the composites show virtually no wear. For conditions of relatively high transverse sliding speeds, a thin film of epoxy forms due to interfacial forces and high surface temperatures arising in relative sliding. As seen in Figure 1, this film tends to cover the ends of the graphite fibers, and acts as a solid film lubricant. For the minimal wear that does occur, the epoxy film appears to peel off in thin wear sheets suggestive of delamination. Figure 2 shows a composite view of surface and subsurface features, and clearly demonstrates the existence of the epoxy layer. Figure 3, taken at 9,000 X, indicates the process by which the epoxy resin flows from within the matrix to form the surface film.

C. Steels

AF-1410 steel was tested in two microstructural conditions. This steel (a modified HY 180), is a weldable, fracture-resistant, high strength alloy developed for airframe structural applications. For purposes of wear testing, the material was double austenitized, quenched at each interim, and appropriately aged to obtain the desired micro-structure. In one case, the aging was conducted to obtain the maximum strength condition ("strong"), while in the other, the material was aged to yield the maximum toughness condition ("tough"). Specimens from both microstructural conditions were tested in compound impact at both low

velocity (1.4 fps) and high velocity (12.2 fps). Peak normal impact stress levels for these two series were 980 psi and 6100 psi, respectively.

Weight loss curves as a function of number of cycles of impact for the high speed series are shown in Figure 4. These results demonstrate that "two body" wear is occurring for this material in both microstructural conditions. The impact caps (counterface material), in fact, suffer considerably more wear than do the specimens. Further, one notes that the "tough" microstructure is more wear resistant than the "strong", and also produces less wear on the counterface.

Surface and subsurface microscopy reveals several features of importance for these high velocity test series. Figure 5 shows a representative "tough" specimen surface following 50,000 cycles of impact loading. Higher magnifications of surface features give insight into the operative wear mechanisms. Figure 6, for example, shows both evidence of plowing (the relatively smooth wear groove) and adjacent areas suggestive of delamination with characteristic layering. Figure 7, on the other hand, is suggestive of delamination alone, with a laminar wear particle lifting from the surface, and about to "peel off". Figure 8 conclusively demonstrates the layering phenomenon, of which more will be said later.

But surface features alone are insufficient to determine whether the delamination mechanism, as postulated in the theory [6], is operative. Figure 9 shows a subsurface section of a "strong" specimen following 150,000 loading cycles. The lath martensite orientation indicates the high degree of subsurface plastic deformation which has occurred, yet

there is no evidence of voids or cracks in this region. The surface layer itself is of considerable interest. One notes an almost structure-less zone which is thought to be a highly refined recrystallized layer. There appears to be some suggestion of cracks within this layer, and on the interface between it and the severely plastically deformed substrate. More will be said later concerning these subsurface zones.

The low velocity test series for the AF-1410 steels yielded several results of significance. First, "two body" wear was observed, in which both specimen (AF-1410) and counterface (impact cap) experienced considerable wear. The counterface material is a 17-4 PH stainless steel, and is described in more detail below. From Figure 10, one notes that the 1410 steels produced several times more counterface wear than did the titanium alloys, and orders of magnitude more wear than did the aluminum alloys. Indeed, for the 1410 steels, the counterface wear well exceeded the specimen wear, suggesting that the 1410 steels be considered as good wear resistant materials.

In addition, as can be seen in Figure 11, the 1410 specimens demon-strate significantly different wear rates. The 1410 "strong" shows an initially high wear rate up to 50,000 load cycles, with a very modest, steady state wear rate up to 160,000 cycles. In contrast, the 1410 "tough" possesses very modest wear up to 75,000 cycles, with an increasing wear rate up to 160,000 impact load cycles. At this outer limit for this test series, the actual specimen wear overlaps for these two micro-structures at 160,000 cycles. From both Figures 10 and 11 it is clear that microstructural variables play an important role in impact wear.

The counterface material utilized in all tests with all specimen materials is 17-4 PH. This material can be broadly classified as a

precipitation hardening martensitic stainless steel. Following the finding that this material was subject to considerable wear with particular specimen materials (most notable the 1410 steels, but also the titanium alloys), surface and subsurface microscopy were conducted on selected impact caps. Figure 12 shows a surface micrograph of such a counterface when run against 1410 "tough" in high speed sliding impact for 150,000 load cycles. In this photo, the base 17-4 PH material can be seen as the bottom surface of a crater from which a wear particle has been plucked. The surrounding zones indicate plowing striations and a large laminar particle layered over this plowed region. These features, taken together, suggest that some material transfer is occurring between specimen (1410) and counterface (17-4 PH).

Subsurface microscopy on impact caps is in progress. Preliminary findings from a low velocity 1410 test show evidence of a thin surface layer on the impact caps, but there is no evidence of void or crack formation, nor even any significant subsurface plastic deformation in the impact cap substrate.

D. Titanium Alloys

Two titanium alloys were tested in both high and low velocity compound impact series. The alloys are IMI 685 and RMI 5522S; the compositions of these alloys have been reported earlier [1], as have some preliminary results [7]. Both of these alloys have been developed for high temperature service, in which strength and creep resistance are important.

For purposes of wear testing, the materials were processed as follows. The RMI 5522S was received as 1/2 inch diameter swaged rod, and was not heat treated in order that a microstructure consisting of

large amounts (about 90%) of continuous elongated primary alpha might be tested for impact wear resistance. While this microstructure is far from optimum in terms of high temperature creep resistance, it represented an unknown in terms of wear resistance.

The IMI 685 alloy, on the other hand, was processed to its re-commended microstructural condition, consisting of nearly 100% trans-formed beta. This material was received as 1 inch diameter rod, and was subsequently swaged to 1/2 inch diameter; it was then beta annealed, quenched, and heat treated to produce the typical "basketweave" micro-structure.

In high velocity compound impact testing, the IMI 685 alloy showed only a minor velocity dependence, while the RMI 5522S demonstrated a significant dependence as seen in Figure 13. The peak normal stress for this test was 1500 psi, and it is found that more wear occurs at the lower transverse sliding velocity (10.5 fps) than at the higher (17.5 fps). While this finding conflicts with results obtained in ballistic impact wear studies [8], it agrees with recent results in pure sliding wear (no impact) obtained with commercially pure titanium at high sliding speeds [9]. In this latter study, wear rates were found to exhibit both a minimum and a maximum within a range of sliding velocities. Between 1.3 and 3.3 fps, the wear rate decreased; between 3.3 and 16.4 fps, the wear rate increased; and as the sliding speed was increased from 16.4 to 32.8 fps, the wear rate again decreased.

It must be appreciated that in this regime of high speed sliding, significantly high surface temperatures are generated, both in sliding and compound impact wear. Indeed, both in [9] and in our own work with

titanium alloys, sparks are observed during testing. These high surface temperatures are thought to lead to a local softening of the specimen surface, with a concomitant reduction in frictional force at the interface. Thus, at the higher sliding velocity, reduced friction is believed to account for the lesser degree of wear observed. This reasoning, however, cannot be extrapolated to a low velocity test series, where thermal effects are less significant.

Figure 14 is representative of the surface appearance of both titanium alloys following high speed sliding impact. While the flat sheets are suggestive of delamination, there is also the plowing groove network superposed. It is possible, indeed, that the flat particles are those which have been back-transferred from the counterface, and have been pounded to shape during impact.

More interesting are the subsurface photomicrographs from the high speed sliding tests. Figure 15 is at relatively low magnification and shows the specimen sectioned parallel to the sliding direction. One notes a leading and a trailing edge of material which indicate the high degree of plastic deformation which occurs. Figure 16, a higher magnification view of the same material (IMI 685), shows a plastically deformed surface layer which contains a swatch of material which is almost broken free. Figure 17 is a subsurface section from RMI 5522S and demonstrates the three zones typically found in such examinations. The deep substrate consists of the unaffected microstructure (zone 1). The intermediate layer is plastically deformed, and this deformation is typically observable in the microstructure (zone 2). Often a refinement in this microstructure can be observed as the near-surface layer (zone 3) is approached. Zone 3 is thought to be a severely plastically deformed, recrystallized layer. In this case, obvious voids and cracks are visible in zone 3.

In the low velocity test series on the titanium alloys, transverse sliding speed was 1.4 fps and peak normal stress level was 980 psi. As noted earlier, both titanium alloys gave rise to counterface wear, but not to the degree that the AF-1410 steels did (Figure 10). Also as noted earlier (Figure 11), the titanium alloys exhibited considerable wear in the low velocity test series. Indeed, these materials (and aluminum alloy 2011-T3) were subject to significantly higher wear rates than 2124 aluminum, the AF-1410 steels, and the graphite epoxy composites (not shown in Figure 11 as the wear curve is indistinguishable from the abcissa).

Surface microscopy for the low speed sliding impact test series reveals little difference from results observed in high speed compound impact. Figure 18 is representative for low speed, and should be compared to Figure 14 for high speed. Subsurface results are also similar between low and high speed sliding, as seen in Figures 19 and 20. Figure 19 shows the RMI 5522S alloy, where again the three characteristic zones can be observed, while Figure 20 shows the IMI 685 alloy at high magnification. This material showed virtually no observable subsurface features from the low speed test series.

Taken together, and noting significant transfer films and counter-face wear, it appears that not only delamination but also adhesive and plowing mechanisms are operative with these titanium alloys over the range of compound impact parameters explored.

E. Aluminum Alloys

Two aluminum alloys have been tested in both low and high speed compound impact. The alloys are 2124 and 2011-T3. The 2124 is a wrought product consisting of aluminum-copper solid solution with a dispersion of intermetallics contained within the relatively soft, tough matrix.

This alloy also possesses very good fracture toughness, particularly in the short transverse direction from which impact specimens were machined. An alternate designation for 2124 is 2024-T851.

The 2011-T3 alloy is a extruded product which consists of aluminum-copper solid solution matrix in which there are dispersed particles of lead and bismuth. This alloy is "free machining", as the soft, low melting point lead and bismuth constituents bond poorly to the matrix and act as incipient voids or crack initiators.

High speed sliding tests with these alloys were conducted at a variety of velocities and peak stress levels. Sliding velocities ranged from 8.7 to 19.2 fps; peak stress levels ranged from 610 to 3260 psi. Wear rates were quite high for the 2011-T3 and moderate for the 2124.

Surface SEM photomicrographs for the two alloys are virtually interchangeable. Accordingly, only those from the 2124 alloy are presented. Figure 21 shows a relatively low magnification view of the surface of a specimen run at 19.2 fps for 50,000 load cycles. On this level, the wear mechanism appears to be abrasive as evidenced by the deep plowing grooves. At increased magnification, however, as seen in Figure 22, there is evidence of layering and of flat, lamellar particles. Figures 23 and 24 show such features at higher magnifications.

Subsurface micrographs for this 2124 alloy are shown in Figures 25 and 26. Figure 25 is typical for this material, and subsurface features are difficult to distinguish in the scanning electron microscope. There is little evidence of a region of large plastic deformation (zone 2), although some flow patterns can be distinguished. The near-surface region (zone 3) is again clearly demarked, and Figure 25 suggests that it is separated from zone 2 by a propagating crack. Figure 26 shows a

dark field image from the light microscope. This photo clearly indicates the gross plastic deformation which has occurred in producing the curled "wear lip" on the trailing edge of the specimen.

But while there is an apparent absence of subsurface features in the 2124 alloy, the 2011-T3 contains an abundance. Figure 27 is a photo taken at 400X from a specimen run at a sliding velocity of 17.5 fps and peak normal impact stress of 2450 psi at 250,000 load cycles. This subsurface section is normal to the sliding direction, so that sliding occurred into the photo. The curvature of the surface is due to the more macroscopic undulations observable as "plowing grooves" at lower magnifications. One notes the appearance of numerous voids and cracks in the near-surface zone.

Figures 28 and 29 show these features in more detail. Figure 28 is a section taken parallel to the sliding direction, where sliding occurred from right to left. One notes numerous voids and cracks, suggestive of subsurface features found in support of the delamination theory of wear. Figure 29 is again normal to the sliding direction, and here it appears that one near-surface zone has been deposited over another.

Figure 30 shows another section parallel to the sliding direction, and again cracks run essentially parallel to the surface. Figure 31 is included to demonstrate the non-uniformity of subsurface features. In this micrograph, there is a comparative absence of the marked void and crack features noted above. However, one notes a distinct near-surface layer which appears to be separating from the plastically deformed zone 2. Figure 32 shows a parallel section from a specimen which was run for only 10,000 cycles. Thus, one finds significant subsurface void and crack formation in the 2011-T3 alloy after a relatively few impact load cycles.

The low speed sliding tests with the aluminum alloys result in similar findings. As shown in Figure 10, virtually no wear of the counterface (impact caps) occurs with either alloy. And, as depicted in Figure 11, the 2124 alloy is considerably more impact wear resistant than is the 2011-T3.

All of these results are those which one would expect from a consideration of the microstructures of the two alloys. While the 2124 is formulated for high fracture toughness, the 2011-T3 is designed to facilitate crack formation. The subsurface features observed correlate with these differences in microstructure, and the observed differences in wear rates likewise correlate.

F.   Reproducibility

A series of tests were undertaken to determine the scatter in weight loss data in compound impact. Specimens of 5/32" diameter 2011-T3 alloy were run at peak impulsive stress of 1566 psi with transverse velocity of 8.7 fps. Results were obtained from three to six specimens at each of the following number of impact load cycles: 10,000; 50,000; 100,000; 250,000. A typical example of the spread of data is at N = 100,000 load cycles. Here, the mean of six data points is 0.01025 g., and the standard deviation is 0.00260 g.

G.   Velocity Dependence

Figure 33 presents weight loss data for the 2011-T3 alloy at two transverse sliding velocities, v = 5.5 fps and v = 8.7 fps. As above, specimen diameter is 5/32" and peak impulsive stress is 1566 psi.

The observations are that more wear occurs at the lower relative sliding speed, and that weight losses increase with increasing numbers of impact cycles. These results correspond to those obtained with titanium alloys.

H.   Stress Dependence

A special test series was undertaken to determine the effect of peak impact stress on the wear rate of aluminum 2011-T3. In this series, the peak impact force was maintained at a constant value of 75 pounds and the relative sliding velocity was likewise maintained constant for all tests at 17.5 fps. By changing specimen diameters, different peak impact stress levels were imposed. Figure 34 shows some results from this series, and the stress dependency is obvious: wear increases with increasing stress.

The data from this test series are plotted as change in height of the specimen as a function of number of load cycles. This is done for the following reason. If one considers weight loss (or volume change), the larger diameter specimens would lose more weight (or volume) per unit thickness worn away than would the smaller. Thus, the height change is more indicative of the amount of wear, and is the quantity of practical importance as well. Weight loss comparisons are significant when one is comparing similar materials of the same geometrical shape (such as two titanium alloys of the same diameter). But when one attempts to draw comparisons between materials, or between specimens of different diameter, height change is the significant variable.

I.   Miscellaneous Tests

In addition to test results noted above, other avenues have been and are being pursued. These are briefly noted below.

Profilometry has been employed in two areas. One such investigation concerned the determination of surface roughness of specimens in various stages of wear. Another utilization of the profilometer is in obtaining wear data for the graphite epoxy composites. These materials are exceedingly

difficult on which to perform weight loss measurements. This is due to the fact that they absorb water from the atmosphere. Accordingly, in some instances we have utilized round nosed (spherically ended) specimens which develop a flat upon wear testing. Profilometer measurements allow calculation of the worn volume, from which comparisons between the composites and other materials may be drawn.

Other areas of experimentation include the measurement of specimen surface temperatures. This is being accomplished by means of thermocouples embedded in a test material just under the wear surface. As the wear process progresses, the thermocouple junction nears the actual wear surface. Finally, the junction becomes a part of the surface, and the test self-destructs. In the process, however, one obtains data on temperatures in and on the wear surface. It is felt that such measurements are important, and due to the wide variations reported in the literature, analytical methods are thought to be unreliable.

Also in progress are test series on two additional materials. These include precipitation-hardening copper-chromium alloys aged for different periods of time to produce differing second-phase particle structures. Similar tests will be done with spherodized 1045 steel. These materials will contain varying volume fractions of second-phase particles, and the particles themselves will vary in size and spacing. Quantitative metallography will be conducted in concert with these test series in order to attempt to obtain quantitative measures of void and crack formation.

Summary of Experimental Results

From the results obtained to date, we can note several important generalizations. First among these is the importance of external variables in the impact wear process, including peak impulsive stress levels and

relative transverse sliding velocity. Secondly, it is clear that different materials possess widely varying impact wear resistance which would not be inferred from simple comparisons of hardness, creep resistance, or the like. Within a given category of materials, microstructural variables are most significant. Thus, one should in principle be able to work toward a material structure most favorable for impact wear resistance, and perhaps by extension, to wear resistance in other forms of loading.

With metallic materials, subsurface phenomena appear to be significant. In general, one observes three characteristic zones beneath the wear track. The zone furthest from the wear surface ranges from unaffected microstructure toward observably deformed "grains". The intermediate zone consists of material which has been subject to exceedingly high plastic deformation, but the basic "grain" structure is still observable, although deforming and refining into flow lines. The near-surface zone is still more plastically deformed, and probably consists of material both from the specimen and that deposited from the counterface. It appears to be highly refined and homogenized, and preliminary TEM results of our own indicate it to be crystalline.

Investigations by other workers have recently been conducted on such near-surface layers arising in simple sliding (no impact) wear [10-12]. Both Bill [10] and Van Dijck [11] find this zone to be crystalline, as distinct from the amorphous Beilby layer which results from polishing and is often cited in the literature. In particular, Van Dijck finds the smallest grains ever measured, ranging in thickness from 200 to 600 $\overset{\circ}{A}$. Moreover, the plastic deformations in this layer are likewise the largest ever measured, ranging up to strains of 230.

Clearly, the formation and properties of these zones occurring in impact wear need further study.

Analytical

During the second phase of our work, a more realistic analytical description of the wear test and a better physical interpretation of the analysis was achieved. As noted earlier [1], we are dealing with "controlled" impact differing from various forms of free (or ballistic) impact considered by others.   In essence, our impact wear testing machine forces the specimen to strike the transducer, which may be stationary or rotating transverse to the direction of normal approach. This forced contact is "controlled" in the sense that the specimen is driven forward by means of the spatial mechanism of the impact wear machine [13]. The dynamic characteristics of the spatial mechanism, which vary depending upon several adjustments made for specific materials and specific test conditions, serve to interact with the dynamic response characteristics of the transducer counterface and its mountings. In short, the impact is "controlled" as compared to the "free" impact that would be characterized by a ballistic device, or a free-fall device.

Accordingly, the analysis is complicated by the fact that the motion of the far end of the specimen is not known exactly, due to the dynamic response characteristics of the overall system, and the existence of tolerances between moving components. Hence, the unknown motion characteristics of the far end of the specimen must be determined. This is possible, by means of a rather complicated procedure developed by Solecki during the first phase of our work. Thus, the initial analysis dealt with the impact of a homogeneous one-dimensional, finite elastic rod [14] upon an elastic half-space (Figure 35). In this work, it was assumed that the far end of the rod was subjected to a prescribed motion due to a controlled impact. The friction between the rod and the half-

space was disregarded in order to avoid dynamic bending of the rod in addition to the propagation of longitudinal stress waves. The objective of this preliminary work was to investigate procedures useful when considering the impact of a 3-dimensional body and to acquire a better understanding of the mechanical behavior of a system under conditions of controlled impact. This work is now in a final stage leading to numerical results, some of which have been reported earlier [1]. The main points of the theory, an explanation of adopted techniques, and the derivation of analytical relations are briefly described in Appendix 2.

It was found [see Appendix 2] that the displacement of an arbitrary point of the rod, $u(x,t)$, is given by the expression

$$u(x,t) = \frac{2L}{\pi^2} V\, A(x,t)\sqrt{\rho/E} + \{f[t-x\sqrt{\rho/E}] - f[t-(2L-x)\sqrt{\rho/E}]+\ldots\}$$

$$+ \{w[t-(L-x)\sqrt{\rho/E}] - w[t-(L+w)\sqrt{\rho/E}]+\ldots\}$$

where f is the "controlling function"; w is the displacement of the striking end; $\sqrt{E/\rho}$ is the speed of elastic wave propagation; V is the velocity of the rod at the instant of the impact and $A(x,t)$ is a bi- or trilinear function of x and t. An inspection of this expression reveals qualitatively the nature of the state of stress during the controlled impact. The first term on the right hand side, proportional to the velocity of the impact, is responsible for generating two rectangular stress waves: a compression wave propagating from the striking end and a tension wave propagating from the far end. These waves are reflected from the opposite ends (changing sign at the far end) and continue propagating until the separation time. This results in periodically oscillating stress at any cross-section of the rod. The second element in this expression, represented by the collection of terms in the first

brackets, describes a finite series of "signals" generated at the far end by the controlling function, $f(t)$. The effect of this is a train of **stress** waves transmitted continuously by the far end until the time of separation occurs. If the duration, t_1, of the contact is large compared to the traverse time, T, of the elastic wave, then the maximum stress resulting from this second element differs only slightly from the static stress. The last element (collection of terms in the second brackets) is similar in its form to the second term and describes the effect of the elastic flexibility of the support. Thus, a sequence of stress waves originating from the striking end tends to decrease the pressure (or tension) generated by the controlled motion of the far end. It is worth emphasizing that in the case of the controlled impact, the velocity, V, is not an independent quantity but is rather the time derivative of the function $f(t)$ at the instant of the impact. Hence the first two elements are closely related and a simplified analysis indicates that the importance of the first "impact" term is amplified relative to the second term as the duration time of the contact decreases.

The three-dimensional, cylindrical model of the striking specimen will have, of course, a different stress distribution than that in the rod. This is due, in part, to the presence of shear waves, reflection of waves from the curved surfaces of the cylinder, dispersion, etc. Nonetheless, the basic character of the physical process will be qualitatively the same as that described above.

It is also expected that a quasi-static counterpart of this three-dimensional model will have a similar stress distribution at the striking end. Thus, during the second phase of our work, our primary effort was concentrated in the following quasi-static problem. A finite, homogeneous, isotropic, elastic flat-ended circular cylinder is subjected to a given

displacement at the upper end (constant vertical component of the displacement; the remaining components equal to zero). The lower end impacts upon a moving, rough, rigid half-space. The roughness of the half-space generates tangential stresses due to friction, while the vertical component of the displacement equals zero (Figure 36). Since this problem is not axially symmetric, it's solution involves considerable difficulties. The Papkovich-Neuber functions were used (for a detailed explanation of the technique, see Appendix 1) to achieve partial uncoupling of Navier's equations of equilibrium in a polar coordinate system. This was followed by double finite Fourier transformation with respect to θ and z resulting in complete uncoupling and in solution of the transformed differential equations. Application of the boundary conditions at the stress-free curved surface of the cylinder and of the conditions at its flat ends leads, after numerous, extremely cumbersome rearrangements to a system of Fredholm's integral equations of the first kind.

The resulting stress distributions are expected to correlate with experimental observations of sub-surface plastic deformation and void and crack formation. For at least some materials, these phenomena are thought to be intimately related to the formation of wear debris.

References

[1] Rice, Stephen L., and Solecki, Roman. Wear of Homogeneous and Composite Materials under Conditions of Repeated Normal and Sliding Impact. AFOSR-TR-77-0857. (1977).

[2] Rice, Stephen L., Reciprocating Impact Wear Testing Apparatus, Wear, 45, 1 (1977) 85-95.

[3] Bair, H. E. and Johnson, G. E., Calorimetric Analysis of Water Clusters in Polyethylene, Bell Telephone Laboratories. (1976).

[4] Johnson, G. E., Bair, H. E., Anderson, E. Q. and Daane, J. H., The Nature of Water in Polyethylene and its Relationship to Dielectric Loss, 1976 Annual Report, Conference on Electrical Insulation and Dielectric Phenomena (NAS-NRC), Bell Laboratories. (1976).

[5] Rice, Stephen L. Impact Wear of Graphite Epoxy Composites. Proc. 2nd. Intl. Conf. on Solid Lubrication (to be published).

[6] Suh, N. P., The Delamination Theory of Wear, Wear, 25, (1973), 111-124.

[7] Rice, Stephen L., Wear of Materials under Impact Loading. Proc. VII Pan-American Congress of Mech. and Electri. Engrs. (1977).

[8] Engel, P. A., Impact Wear of Materials. Elsevier, Amsterdam. (1976).

[9] Saka, N., Eleiche, A. M. and Suh, N. P., Wear of Metals at High Sliding Speeds, Wear, 44, p. 109-126. (1977).

[10] Bill, R. C. and Wisander, D. W., Recrystallization as a Controlling Process in the Wear of Some F.C.C. Metals, Wear, 41, p. 351-363. (1977).

[11] Van Dijck, J. A. B., The Direct Observation in the Transmission Electron Microscope of the Heavily Deformed Surface Layer of a Copper Pin After Dry Sliding Against a Steel Ring, Wear, 42, p. 109-117 (1977).

[12] Bill, R. C. and Wisander, D. W., Surface Recrystallization Theory of the Wear of Copper in Liquid Methane. NASA Tech. Note D-7840. (1974).

[13] Rice, Stephen L., Impact Wear Testing Machine, Invention Disclosure, University of Connecticut, 1975.

[14] Solecki, R., Controlled Impact of a Finite Elastic Rod on an Isotropic Elastic Half-Space, (to be submitted for publication)
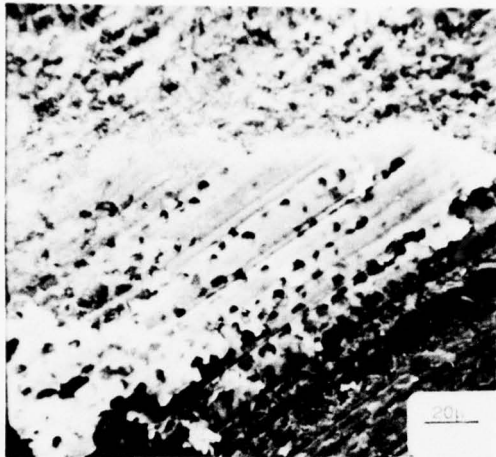
Figure 1: Hercules Composite;
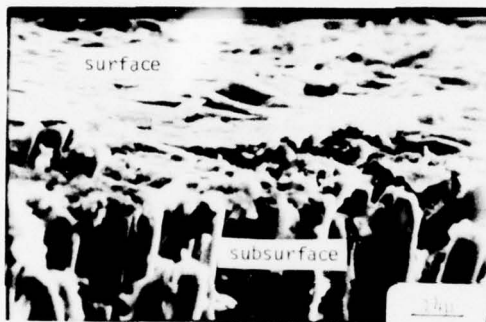V = 1.4 fps;
N = 150,000

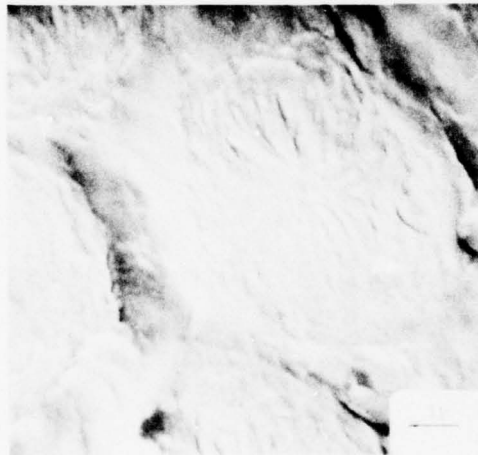Figure 2: Hercules Composite;
V = 17.5 fps
N = 100,000

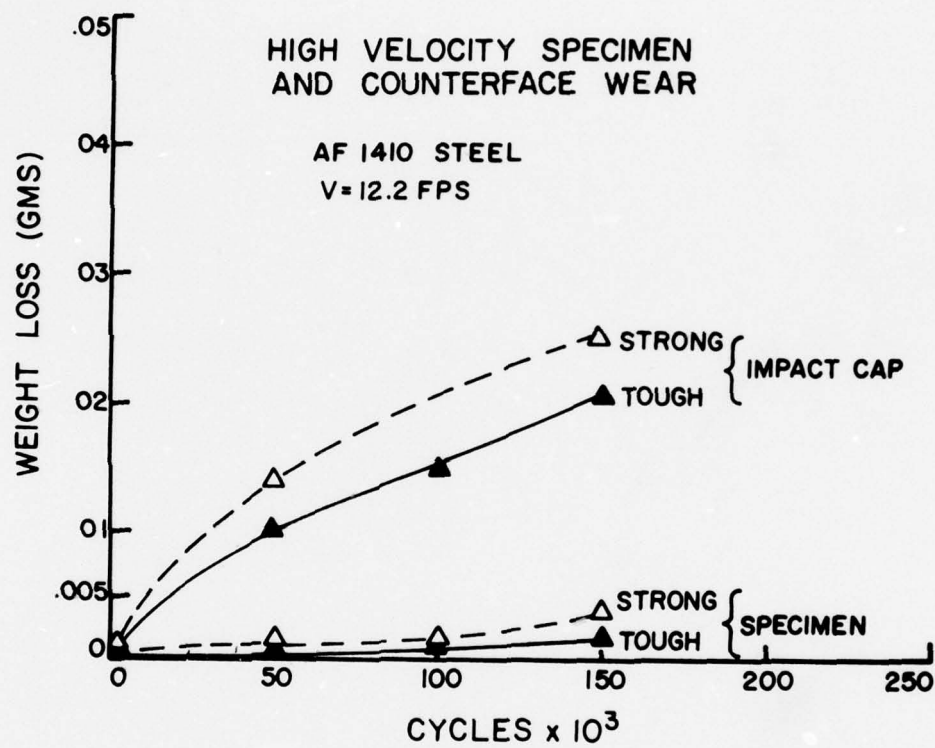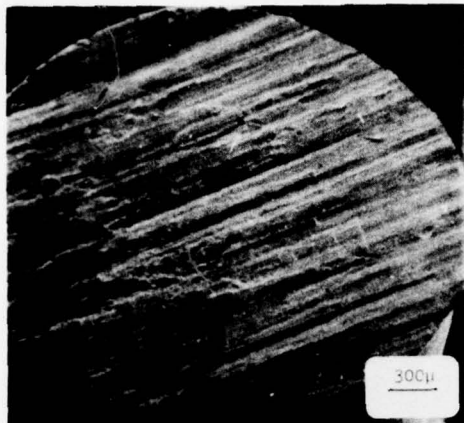Figure 3: Hercules Composite;
V = 1.4 fps;
N = 150,000

FIGURE 4

Figure 5: 1410 Tough;
           V = 12.2 fps;
           σ = 6100 psi;
           N = 50,000

Figure 6: 1410 Tough;
           V = 12.2 fps;
           σ = 6100 psi;
           N = 150,000

Figure 7: 1410 Tough;
           V = 12.2 fps;
           σ = 6100 psi;
           N = 50,000
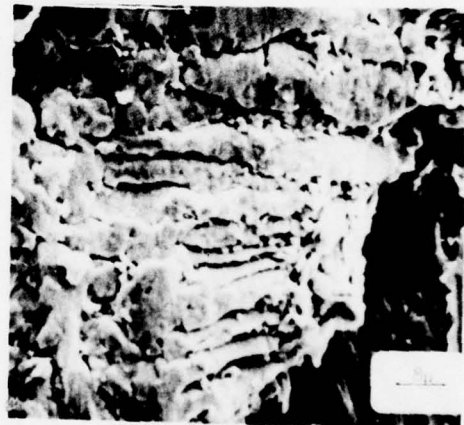
Figure 8: 1410 Tough;
           V = 1.4 fps;
           σ = 980 psi;
           N = 160,000
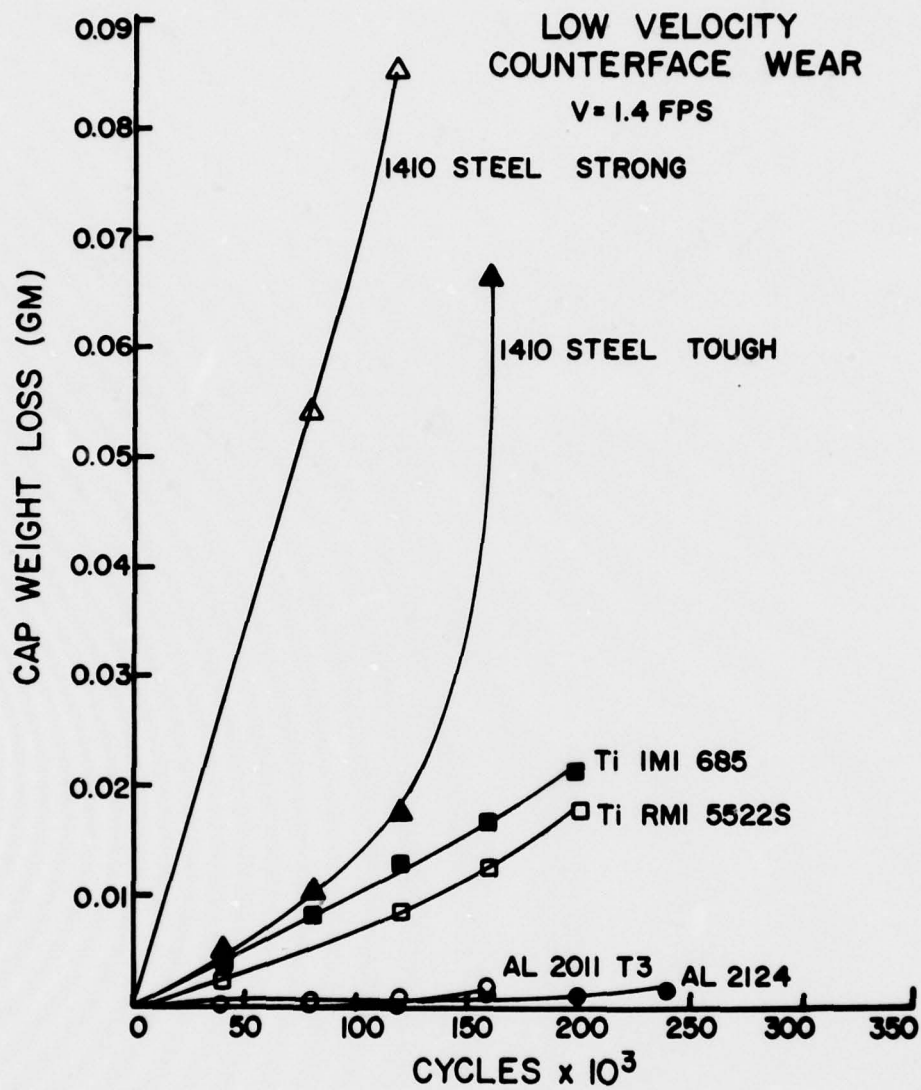
FIGURE 10
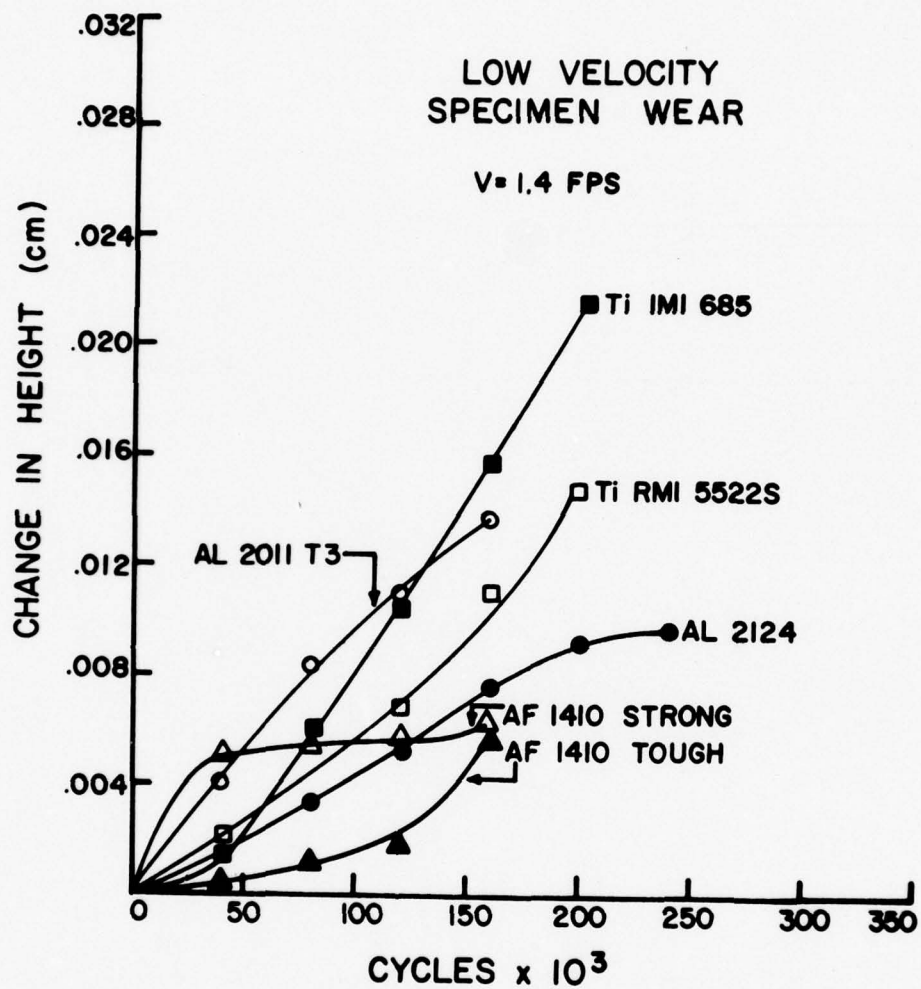
FIGURE 11

Figure 9: 1410 Strong;
V = 12.2 fps;
σ = 6100 psi;
N = 150,000

Figure 12: 17-4 PH Impact Cap;
Worn by 1410 Tough;
V = 12.2 fps;
σ = 6100 psi;
N = 150,000
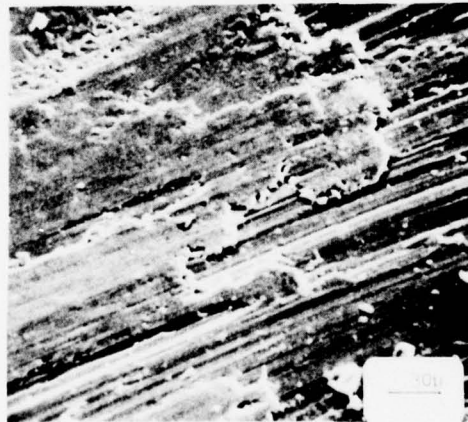
Figure 14: IMI 685;
V = 10.5 fps;
σ = 1530 psi;
N - 50,000

HIGH VELOCITY
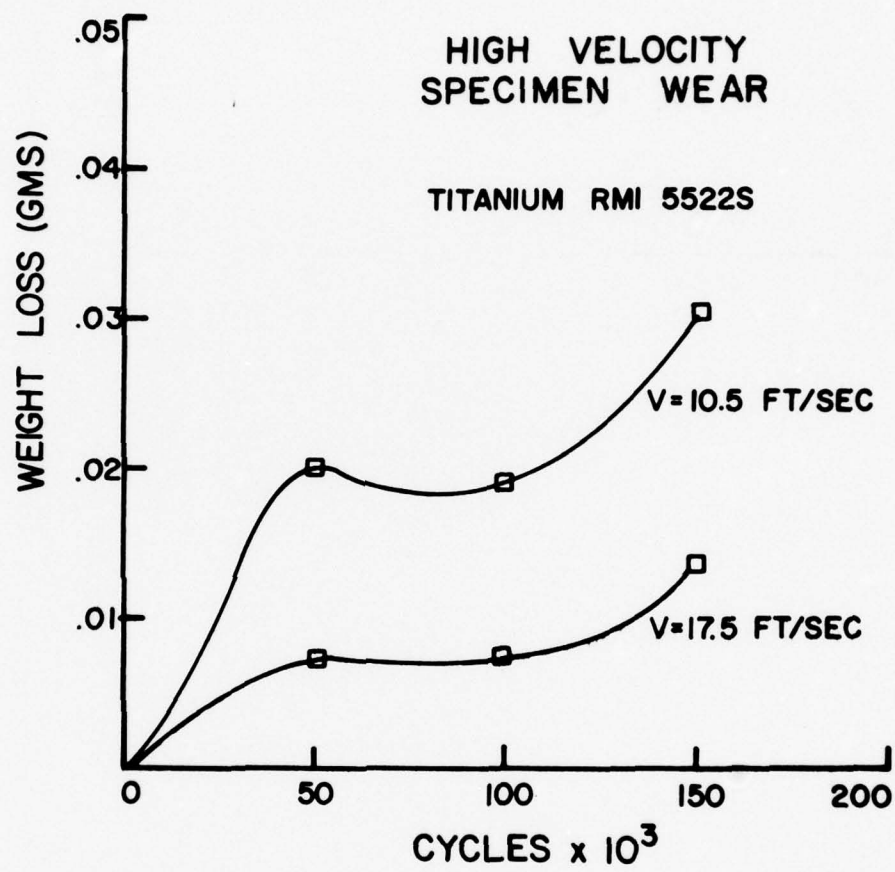SPECIMEN WEAR
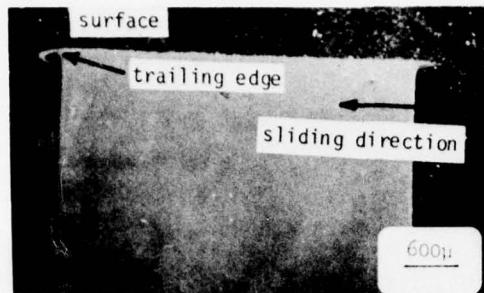
TITANIUM RMI 5522S

WEIGHT LOSS (GMS)

V=10.5 FT/SEC

V=17.5 FT/SEC

CYCLES x 10³

FIGURE 13

Figure 15: IMI 685;
         V = 17.5 fps;
         σ = 1530 psi;
         N = 500,000

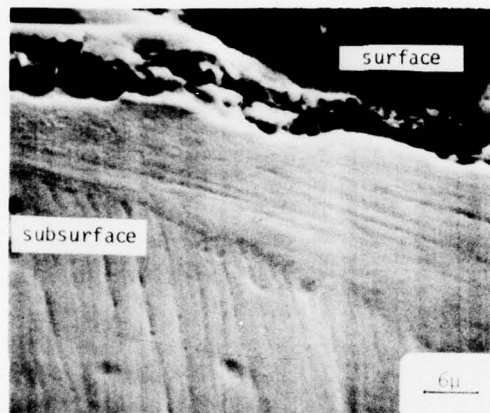
Figure 16: IMI 685;
         V = 17.5 fps;
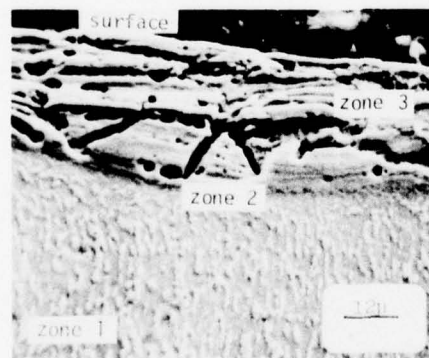   σ = 1530 psi;
         N = 500,000

Figure 17: RMI 5522S;
         V = 17.5 fps;
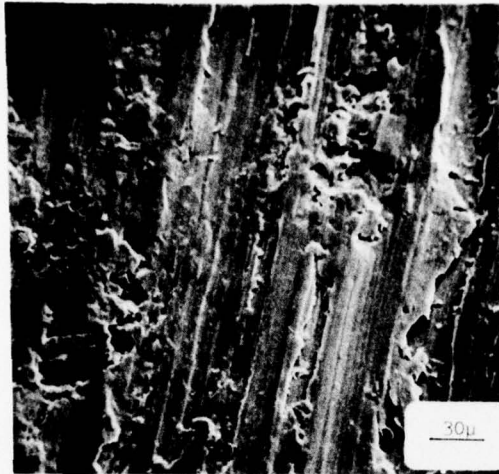   σ = 1530 psi;
         N = 500,000

Figure 18: RMI 5522S;
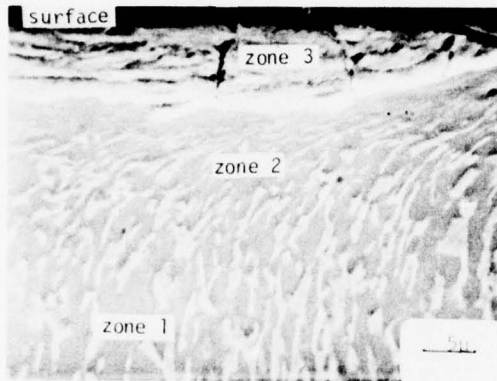V = 1.4 fps;
σ = 980 psi;
N = 200,000

Figure 19: RMI 5522S;
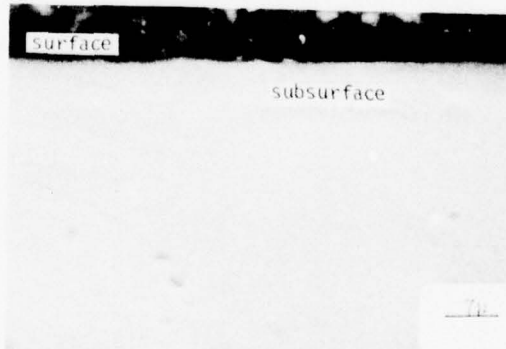V = 1.4 fps;
σ = 980 psi;
N = 200,000

Figure 20: IMI 685;
V = 1.4 fps;
σ = 980 psi;
N = 200,000

Figure 21: 2124;
V = 17.5 fps;
σ = 610 psi;
N = 50,000

Figure 22: 2124;
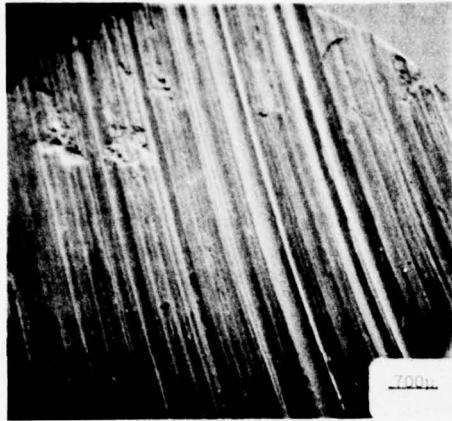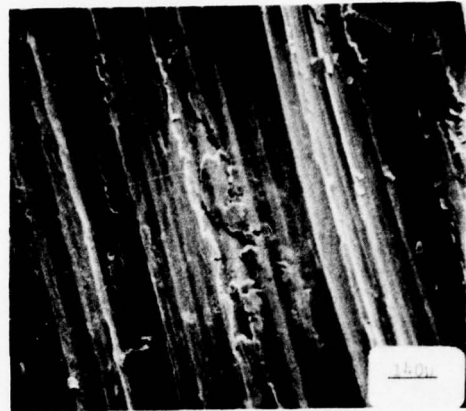V = 17.5 fps;
σ = 610 psi;
N = 50,000

Figure 23: 2124;
V = 17.5 fps;
σ = 610 psi;
N = 50,000
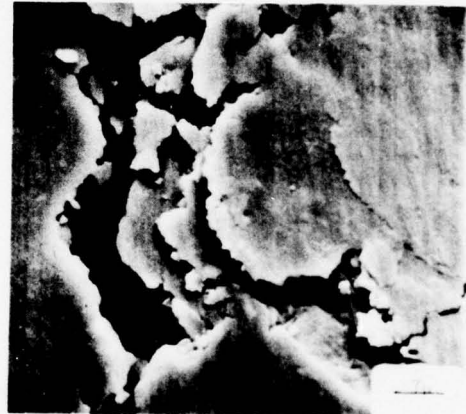
Figure 24: 2124;
V = 17.5 fps;
σ = 610 psi;
N = 50,000
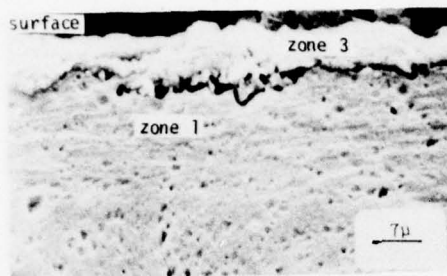
Figure 25: 2124;
V = 17.5 fps;
σ = 610 psi;
N = 150,000
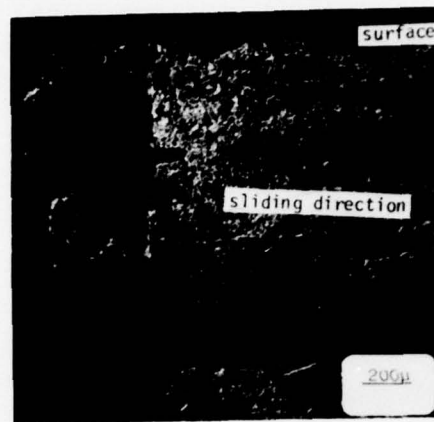
Figure 26: 2124;
V = 17.5 fps;
σ = 610 psi;
N = 150,000
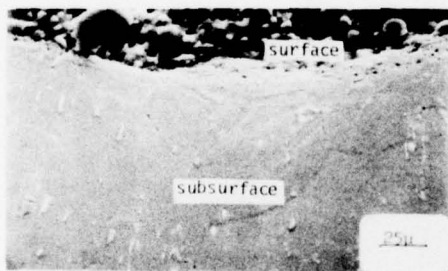
Figure 27: 2011-T3;
V = 17.5 fps;
σ = 2450 psi;
N = 250,000
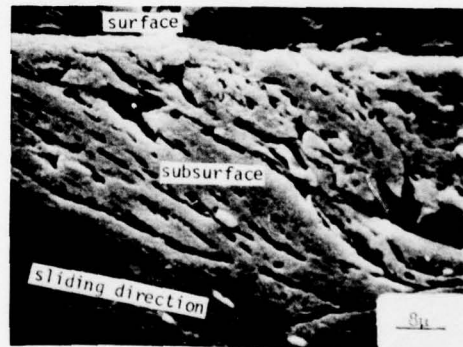
Figure 28: 2011-T3;
V = 8.7 fps;
σ = 2450 psi;
N = 250,000
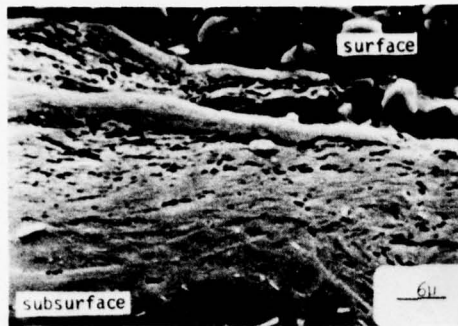
Figure 29: 2011-T3;
V = 17.5 fps;
σ = 2450 psi;
N = 250,000
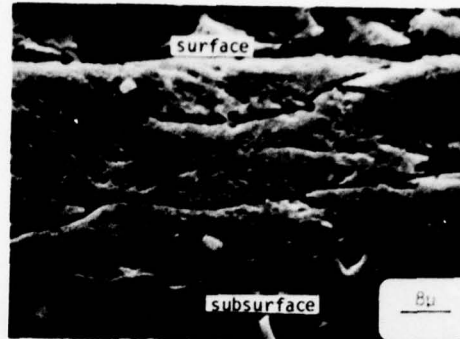
Figure 30: 2011-T3;
V = 8.7 fps;
σ = 2450 psi;
N = 250,000

Figure 31: 2011-T3;
V = 17.5 fps;
σ = 2450 psi;
N = 100,000

Figure 32: 2011-T3;
V = 8.7 fps;
σ = 2450 psi;
N = 10,000

VELOCITY DEPENDENCE
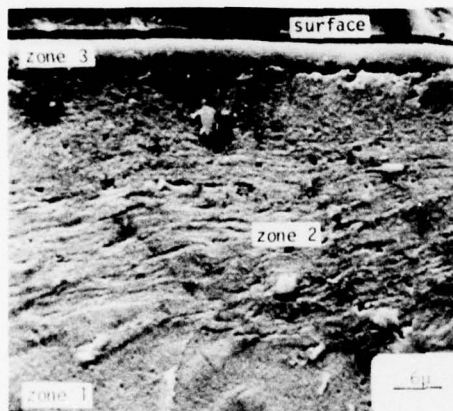
ALUMINUM 2011 T3

V = 5.5 FT/SEC

V = 8.7 FT/SEC

CYCLES x 10^3

WEIGHT LOSS (GMS)
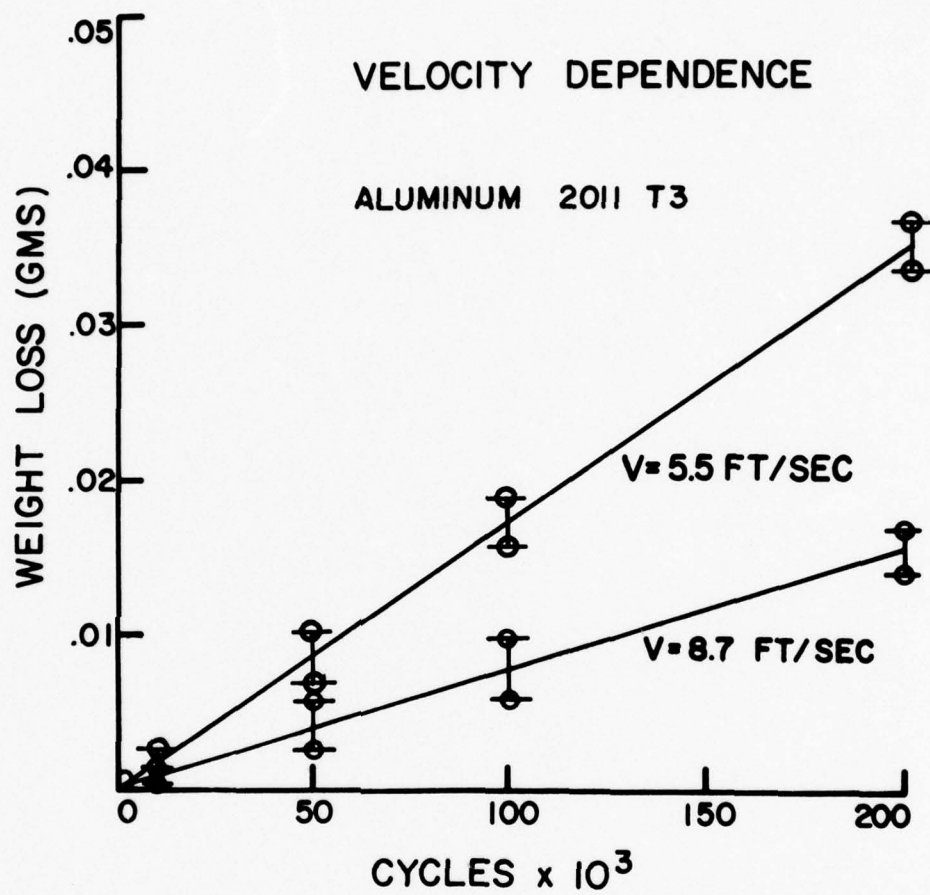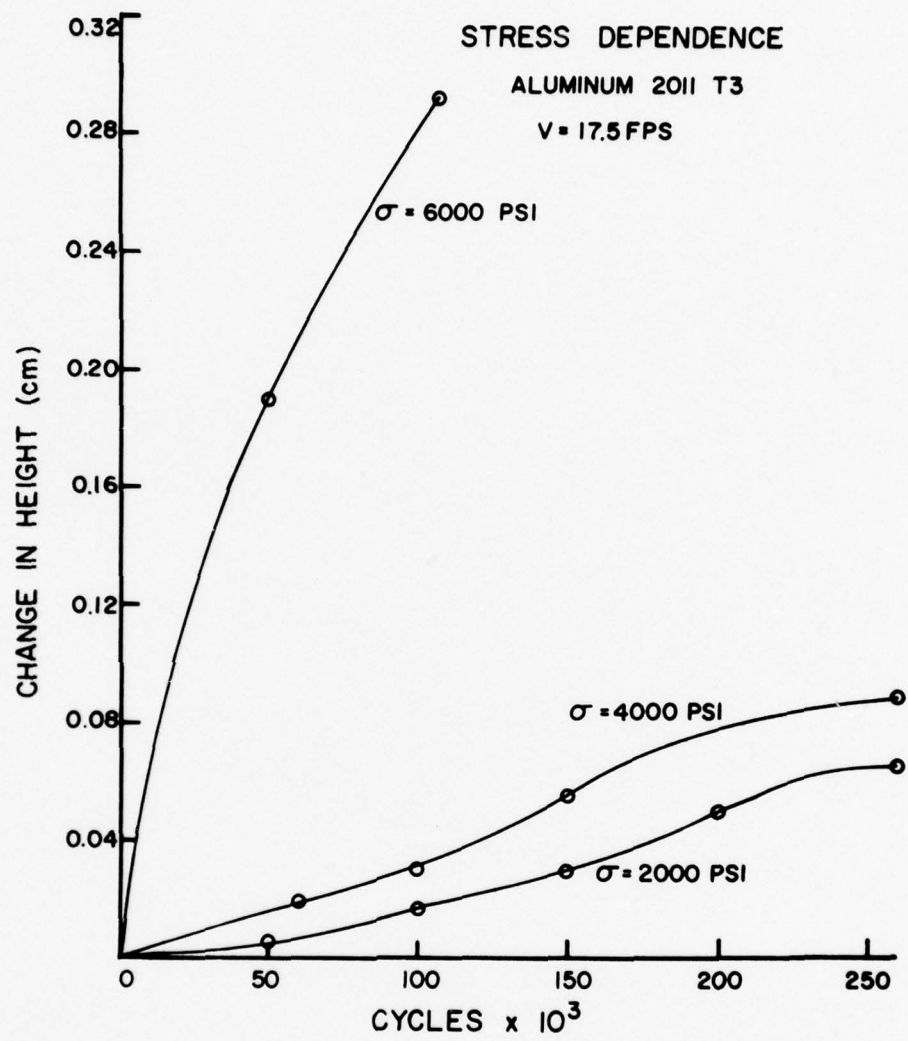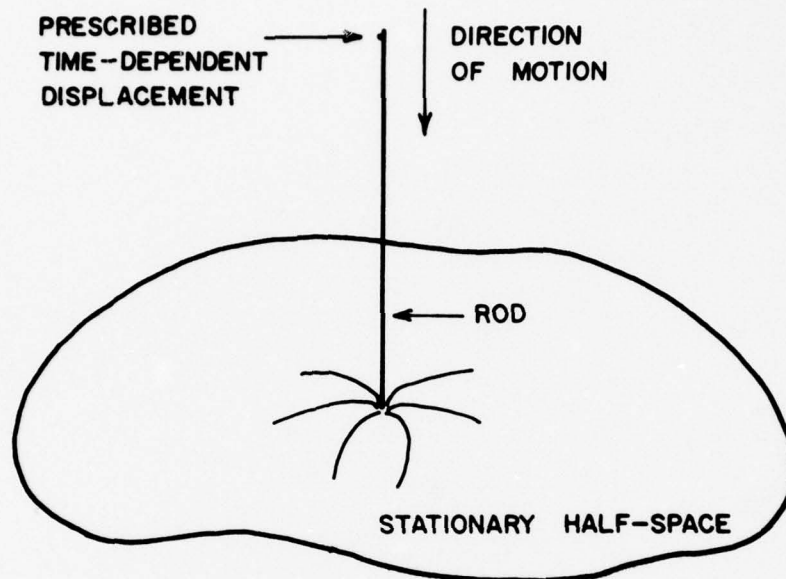
FIGURE 33

FIGURE 34

ELASTIC ROD STRIKES INFINITE ELASTIC HALF – SPACE
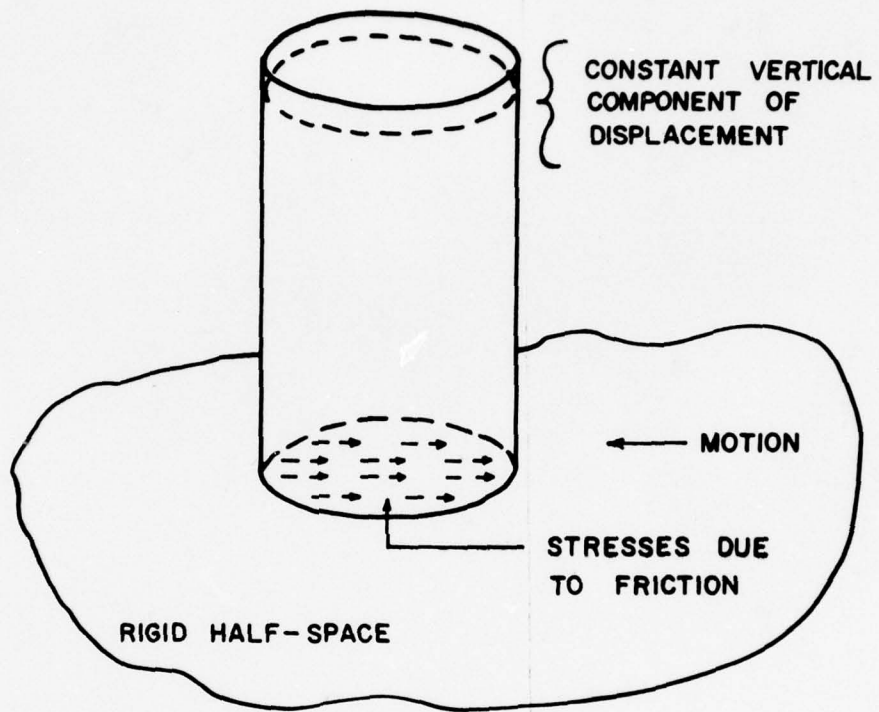
FIGURE 35

QUASI-STATIC DEFORMATION OF AN ELASTIC CYLINDER

FIGURE 36

Appendix 1. The effect of friction on the stress distribution in a finite elastic cylinder.

1. Introduction

In the present paper the effect of friction on the stress distribution in a finite, isotropic, homogeneous elastic circular cylinder is analysed. It is assumed that the curved surface of the cylinder is stress-free. The components of the displacement vector are preassigned at one flat end of the cylinder while at the other end the axial component of the displacement vector is zero. Also at this end the shear component of the stress tensor is either zero (in one direction) or proportional to the normal component of the stress tensor (in the perpendicular direction). The problem is thus not axially symmetric. The Papkovich-Neuber functions are used in order to uncouple the field equations. The dependence of the unknown functions on the angular and axial variables is then eliminated by means of finite Fourier integral transformations. Application of boundary conditions at the flat ends leads to a coupled system of Fredholm integral equations of the first kind where the unknowns are the shear stresses at those ends. Numerical techniques will be employed to solve this system.

2. Solution of the field equations

The differential equations governing the displacements of a homogenous, isotropic elastic, cylinder take the following form in the cylindrical coordinate system (see [1] p. 236).

$$\nabla^2 u_r - \frac{u_r}{r^2} - \frac{2}{r^2} \frac{\partial u_\theta}{\partial \theta} + \frac{1}{1-2\nu} \frac{\partial \Lambda}{\partial r} = 0 \tag{1.1}$$

$$\nabla^2 u_\theta - \frac{u_\theta}{r^2} + \frac{2}{r^2} \frac{\partial u_r}{\partial \theta} + \frac{1}{1-2\nu} \frac{1}{r} \frac{\partial \Delta}{\partial \theta} = 0 \tag{1.2}$$

$$\nabla^2 u_z + \frac{1}{1-2\nu} \frac{\partial \Delta}{\partial z} = 0 \tag{1.3}$$

where u_r, u_θ, u_z are the physical components of the displacement vector $\underset{\sim}{\mu}$, ∇^2 is the Laplacian

$$\nabla^2 = \frac{\partial^2}{\partial r^2} + \frac{1}{r} \frac{\partial}{\partial r} + \frac{1}{r^2} \frac{\partial^2}{\partial \theta^2} + \frac{\partial^2}{\partial z^2} \tag{2}$$

and the dilatation Δ is given by

$$\Delta = \frac{\partial u_r}{\partial r} + \frac{1}{r} (\frac{\partial u_\theta}{\partial \theta} + u_r) + \frac{\partial u_z}{\partial z} \tag{3}$$

The partial uncoupling of the above system succeeds with the help of Papkovich-Neuber substitution [2]

$$\underset{\sim}{u} = \underset{\sim}{\nabla} (\phi + 1/2 \underset{\sim}{r} \cdot \underset{\sim}{\psi}) - 4(1-\nu)\underset{\sim}{\psi} \tag{4}$$

It is assumed without loss of generality ([2] p. 331) that the axial component ψ_z of the vector potential $\underset{\sim}{\psi}$ equals zero and therefore eq (4) written in component form becomes

$$u_r = \frac{\partial}{\partial r} (\phi + r\psi_r) - 4(1-\nu)\psi_r \tag{5.1}$$

$$u_\theta = \frac{\partial}{r\partial \theta} (\phi + r\psi_r) - 4(1-\nu)\psi_\theta \tag{5.2}$$

$$u_z = \frac{\partial}{\partial z} (\phi + r\psi_r) \tag{5.3}$$

The substitution of expression (5) into the Navier equations (1) leads to their partial uncoupling

$$\nabla^2 \Psi_r - \frac{2}{r^2} \frac{\partial \Psi_\theta}{\partial \theta} - \frac{1}{r^2} \Psi_r = 0 \tag{6.1}$$

$$\nabla^2 \Psi_\theta + \frac{2}{r^2} \frac{\partial \Psi_r}{\partial \theta} - \frac{1}{r^2} \Psi_\theta = 0 \tag{6.2}$$

$$\nabla^2 \phi = 0 \tag{6.3}$$

The solutions of eq. 6 are subjected to the following boundary conditions on the curved surface $r = R$:

$$\sigma_{rr} = \frac{1-\nu}{(1+\nu)(1-2\nu)} E \left[4(1-\nu) \frac{\partial \Psi_r}{\partial r} - \frac{\partial^2}{\partial r^2} (\phi + r\Psi_r) \right] + \frac{E}{2(1+\nu)} \left[\frac{4(1-\nu)}{r} \frac{\partial \Psi}{\partial \theta} \right. \tag{7.1}$$

$$\left. - \frac{1}{r^2} \frac{\partial^2}{\partial \theta^2} (\phi + r\Psi_r) + \frac{4(1-\nu)}{r} \Psi_r - \frac{1}{r} \frac{\partial}{\partial r} (\phi + r\Psi_r) - \frac{\partial^2}{\partial z^2} (\phi + r\Psi_r) \right] = 0$$

$$\sigma_{rz} = \frac{E}{1+\nu} \left[2(1-\nu) \frac{\partial \Psi_r}{\partial z} - \frac{\partial^2}{\partial r \partial z} (\phi + r\Psi_r) \right] = 0 \tag{7.2}$$

$$\sigma_{r\theta} = \left[\frac{4(1-\nu)}{r} \frac{\partial \Psi_r}{\partial \theta} - \frac{2}{r} \frac{\partial^2}{\partial r \partial \theta} (\phi + r\Psi_r) - \frac{4(1-\nu)}{r} \Psi_\theta + \frac{2}{r^2} \frac{\partial}{\partial \theta} (\phi + r\Psi_r) \right.$$

$$\left. + 4(1-\nu) \frac{\partial \Psi_\theta}{\partial r} \right] \frac{E}{1+\nu} = 0 \tag{7.3}$$

and the following ones at $z=1$:

$$u_r = \frac{\partial}{\partial r} (\phi + r\Psi_r) - 4(1-\nu) \Psi_r = 0 \tag{8.1}$$

$$u_\theta = \frac{1}{r} \frac{\partial}{\partial \theta} (\phi + r\Psi_r) - 4(1-\nu)\Psi_\theta = 0 \tag{8.2}$$

$$u_z = \frac{\partial}{\partial z} (\phi + r\Psi_r) = C \tag{8.3}$$

At the end $z = 0$ the conditions $\sigma_{zy} = 0$, $\sigma_{xz} = k\sigma_{zz}$ become

$$\sigma_{rz} \sin\theta + \sigma_{\theta z} \cos\theta = 0 \qquad \sigma_{rz} \cos\theta - \sigma_{\theta z} \sin\theta = k\sigma_{zz}$$

wherefrom, after elimination of σ_{rz}, one obtains

$$\sigma_{\theta z} = -k\sigma_{zz} \sin\theta$$

Therefore the conditions at $z = 0$ become finally

$$u_z = \frac{\partial}{\partial z} (\phi + r\Psi_r) = 0 \tag{8.4}$$

$$\frac{E}{2(1+\nu)} [\frac{\partial^2}{r\partial\theta\partial z} (\phi + r\Psi_r) - 4(1-\nu) \frac{\partial\Psi_\theta}{\partial z}] + k \sin\theta \{ \frac{3-2\nu}{2(1+\nu)(1-2\nu)} E$$

$$[\frac{\partial^2}{\partial z^2} (\phi + r\Psi_r)] - \frac{E}{1+\nu} (1-2\nu) \frac{1}{r} [\frac{\partial}{\partial r}(r\Psi_r) + \frac{\partial\Psi_\theta}{\partial\theta}] \} = 0 \tag{8.5}$$

The variable θ is eliminated first by applying finite Fourier sine or cosine transformations:

$$\bar\Psi_r \equiv \bar\Psi_r(r,n,z) \equiv \int_0^{2\pi} \Psi_r(r,\theta,z) \sin n\theta d\theta$$

$$\bar\Psi_\theta \equiv \bar\Psi_\theta(r,n,z) \equiv \int_0^{2\pi} \Psi_\theta(r,\theta,z) \cos n\theta d\theta$$

$$\bar\phi \equiv \bar\phi(r,n,z) \equiv \int_0^{2\pi} \phi(r,\theta,z) \sin n\theta d\theta \tag{9}$$

Applying Fourier sine transformation to (6.1) and (6.3) and Fourier cosine transformation to (6.2) results in the following system of equations:

$$\bar{\nabla}^2 \, \bar{\Psi}_r + \frac{2n}{r^2} \, \bar{\Psi}_\theta - \frac{1}{r^2} \, \bar{\Psi}_r \; = \; 0 \tag{10.1}$$

$$\bar{\nabla}^2 \, \bar{\Psi}_\theta + \frac{2n}{r^2} \, \bar{\Psi}_r - \frac{1}{r^2} \, \bar{\Psi}_\theta \; = \; 0 \tag{10.2}$$

$$\bar{\nabla}^2 \, \bar{\phi} \; = \; 0 \tag{10.3}$$

where

$$\bar{\nabla}^2 = \frac{\partial^2}{\partial r^2} + \frac{1}{r} \frac{\partial}{\partial r} - \frac{n^2}{r^2} + \frac{\partial^2}{\partial z^2}$$

It can be also shown that the condition $u_z = \text{const}$ at $z = \text{const}$ implies that at $z = \text{const}$ also following relations hold

$$\frac{\partial \bar{\Psi}_r}{\partial z} = \frac{1+\nu}{2E(1-\nu)} \, \bar{\sigma}_{rz}$$

$$\frac{\partial \bar{\Psi}_\theta}{\partial z} = \frac{1+\nu}{2E(1-\nu)} \, \bar{\sigma}_{\theta z}$$

$$\frac{\partial \bar{\phi}}{\partial z} = - \frac{1+\nu}{2E(1-\nu)} \, r \bar{\sigma}_{rz} \tag{11}$$

The boundary conditions (7.1) and (7.2) are subjected to Fourier sine transformation with respect to θ while (7.3) is subjected to Fourier cosine transformation yielding at $r = R$:

$$\frac{1-\nu}{1-2\nu} \, [4(1-\nu) \frac{\partial \bar{\Psi}r}{\partial r} - \frac{\partial^2}{\partial r^2} \, (\bar{\phi} + r \bar{\Psi}_r)] + \frac{1}{2} \, [- \frac{4(1-\nu)}{r} \, n \Psi_\theta + \frac{4(1-\nu)}{r} \, \Psi_r$$

$$+ (\frac{n^2}{r^2} - \frac{1}{r} \frac{\partial}{\partial r} - \frac{\partial^2}{\partial z^2}) \, (\bar{\phi} + r \bar{\Psi}_r)] \; = \; 0 \tag{12.1}$$

$$2(1-\nu)\frac{\partial\bar{\Psi}_r}{\partial z} - \frac{\partial^2}{\partial r\partial z}(\bar{\phi} + r\bar{\Psi}_r) = 0 \tag{12.2}$$

$$\frac{2(1-\nu)}{r}n\bar{\Psi}_r - \frac{2(1-\nu)}{r}\bar{\Psi}_\theta + 2(1-\nu)\frac{\partial\bar{\Psi}_\theta}{\partial r} + n(\frac{1}{r^2} - \frac{1}{r}\frac{\partial}{\partial r})(\bar{\phi} + r\bar{\Psi}_r) = 0 \tag{12.3}$$

Fourier sine transforms with respect to θ of (8.1) and (8.3) and Fourier cosine transform of (8.2) have the form:

$$\frac{\partial}{\partial r}(\bar{\phi} + r\bar{\Psi}_r) - 4(1-\nu)\bar{\Psi}_r = 0 \qquad\text{at } z = 1 \tag{13.1}$$

$$\frac{1}{r}n(\bar{\phi} + r\bar{\Psi}_r) - 4(1-\nu)\bar{\Psi} = 0 \qquad\text{at } z = 1 \tag{13.2}$$

$$\frac{\partial}{\partial z}(\bar{\phi} + r\bar{\Psi}_r) = 0 \qquad\text{at } z = 1 \tag{13.3}$$

Finally θ is eliminated from the boundary conditions (8.4), (8.5) by means of Fourier sine transformation:

$$\frac{\partial}{\partial z}(\bar{\phi} + r\bar{\Psi}_r) = 0 \qquad\text{at } z = 0 \tag{14.1}$$

$$\frac{E}{2(1-\nu)}[\frac{n}{r}\frac{\partial}{\partial z}(\bar{\phi} + r\bar{\Psi}_r) - 4(1-\nu)\frac{\partial\bar{\Psi}_\theta}{\partial z}] - k\varepsilon_n\{\frac{3-2\nu}{2(1+\nu)(1-2\nu)}E\frac{\partial^2}{\partial z^2}(\bar{\phi}_{n+1}$$

$$+ r\bar{\Psi}_{r,n+1}) - \frac{E}{1+\nu}(1-2\nu)\frac{1}{r}[\frac{\partial}{\partial r}(r\bar{\Psi}_{r,n+1}) - (n+1)\bar{\Psi}_{\theta,n+1}]\} = 0 \tag{14.2}$$

where

$$\varepsilon_n = \begin{array}{l} 1 \quad\text{for } n = 0 \\ 1/2 \quad\text{for } n \neq 0 \end{array}$$

and where the following notation has been adopted

$$\bar{\phi}_{n+1} \equiv \bar{\phi}(r,n+1,z) \qquad\text{etc.}$$

Elimination of the variable z follows by means of finite Fourier cosine transformation.

We define:

$$\bar{\bar{\Psi}}_r (r,n,m) \equiv \int_0^{\ell} \bar{\Psi}_r (r,n,z) \cos \lambda_m z \, dz \tag{15.1}$$

$$\bar{\bar{\Psi}}_\theta (r,n,m) \equiv \int_0^{\ell} \bar{\Psi}_\theta (r,n,z) \cos \lambda_m z \, dz \tag{15.2}$$

$$\bar{\bar{\Phi}} (r,n,m) \equiv \int_0^{\ell} \bar{\Phi} (r,n,z) \cos \lambda_m z \, dz \tag{15.3}$$

where

$$\lambda_m = m\pi/\ell \tag{16}$$

The transformed field equations (10) become now

$$L_1 \bar{\bar{\Psi}}_r + \frac{2n}{r^2} \bar{\bar{\Psi}}_\theta = G_{1n}(r) - (-1)^m G_{2n}(r) \qquad m = 0,1,\ldots \tag{17.1}$$

$$L_1 \bar{\bar{\Psi}}_\theta + \frac{2n}{r^2} \bar{\bar{\Psi}}_r = G_{3n}(r) - (-1)^m G_{4n}(r) \qquad m = 0,1,\ldots \tag{17.2}$$

$$L_2 \bar{\bar{\Phi}} = -r[G_{1n}(r) - (-1)^m G_{2n}(r)] \qquad m = 0,1,\ldots \tag{17.3}$$

where

$$L_1 = \frac{d^2}{dr^2} + \frac{1}{r}\frac{d}{dr} - \frac{n^2+1}{r^2} - \lambda_m^2 \qquad\qquad L_2 = \frac{d^2}{dr^2} + \frac{1}{r}\frac{d}{dr} - \frac{n^2}{r^2} - \lambda_m^2$$

$$G_{1n}(r) = \frac{1+\nu}{2E(1-\nu)} \bar{\sigma}_{rz}(r,n,o) \qquad\qquad G_{2n}(r) = \frac{1+\nu}{2E(1-\nu)} \bar{\sigma}_{rz}(r,n,\ell)$$

$$G_{3n}(r) = \frac{1+\nu}{2E(1-\nu)} \bar{\sigma}_{\theta z}(r,n,0) \qquad\qquad G_{4n}(r) = \frac{1+\nu}{2E(1-\nu)} \bar{\sigma}_{\theta z}(r,n,\ell) \tag{18}$$

Also the boundary conditions are transformed again to eliminate z. One obtains at r = R:

$$(5-12\nu + 8\nu^2) \frac{d\bar{\bar{\Psi}}_r}{dr} + [-\lambda_m^2 R^2 - (n^2+1) + 2(1-2\nu)^2] \frac{1}{R} \bar{\bar{\Psi}}_r + 8n\nu(1-\nu)\frac{1}{R}\bar{\bar{\Psi}}_\theta -$$

$$- (\frac{n^2}{R^2} + \lambda_m^2)\bar{\bar{\Phi}} + \frac{1}{R}\frac{d\bar{\bar{\Phi}}}{dr} = 2(1-\nu)R[G_{1n}(R) - (-1)^m G_{2n}(R)] \tag{19.1}$$

$$(1-2\nu)\bar{\bar{\Psi}}_r - \frac{d\bar{\bar{\Phi}}}{dr} - R\frac{d\bar{\bar{\Psi}}_r}{dr} = 0 \tag{19.2}$$

$$\frac{n}{R}\bar{\bar{\Psi}}_r + \frac{n}{R^2}\bar{\bar{\Phi}} - 2(1-\nu)\frac{\bar{\bar{\Psi}}_\theta}{R} + 2(1-\nu)\frac{d\bar{\bar{\Psi}}_\theta}{dr} = 0 \tag{19.3}$$

$$m = 0,1,\ldots\infty$$

Note that the conditions

$$\bar{\sigma}_{rz}(R,n,0) = \bar{\sigma}_{rz}(R,n,\ell) = 0 \tag{20}$$

resulting from the absence of the shearing stress on the curved surface have been used here.

Eqs. (17.1) and (17.2) are uncoupled by either adding or substracting (a method applied by Achenbach [1] p. 239). When the resulting equations are solved one gets for $m \neq 0$:

$$\bar{\bar{\Psi}}_r(r,n,m) = C_{1mn}I_{n-1}(\lambda_m r) - C_{2mn}I_{n+1}(\lambda_m r) + \bar{\bar{\Psi}}_{rp}(r,n,m)$$

$$\bar{\bar{\Psi}}_\theta(r,n,m) = C_{1mn}I_{n-1}(\lambda_m r) + C_{2mn}I_{n+1}(\lambda_m r) + \bar{\bar{\Psi}}_{\theta p}(r,n,m)$$

$$\bar{\bar{\Phi}}(r,n,m) = C_{3mn}I_n(\lambda_m r) + \bar{\bar{\Phi}}_p(r,n,m) \tag{21}$$

while for $m = 0$ the differential equations reduce to Euler's equations and their solutions have the following forms:

$$\bar{\bar{\Psi}}_r(r,n,0) = H_{1n}r^{n+1} + H_{2n}r^{n-1} + \bar{\bar{\Psi}}_{rp}(r,n,0)$$

$$\bar{\bar{\Psi}}_\theta(r,n,0) = -H_{1n}r^{n+1} + H_{2n}r^{n-1} + \bar{\bar{\Psi}}_{\theta p}(r,n,0)$$

$$\bar{\bar{\Phi}}(r,n,0) = H_{3n}r^n + \bar{\bar{\Phi}}_p(r,n,0) \tag{22}$$

where $\bar{\bar{\psi}}_{rp}$ and other functions with a subscript "p" are the particular solution defined later.

Using the boundary conditions eq. (19) and denoting

$$Y_{mn} = \bar{\bar{\psi}}_{rp} \ (R,n,m) \qquad\qquad X_{mn} = \bar{\bar{\psi}}_{\theta p} \ (R,n,m)$$

$$T_{mn} = \bar{\bar{\phi}}_{p} \ (R,n,m)$$

and also $Y'_{mn} = \lim d\bar{\bar{\psi}}_{rp} \ (r,n,m)/dr \quad$ as $\ r = R \qquad$ etc. $\hspace{2cm}$ (23)

we obtain after numerous manipulations the following expressions for the constants C_{1mn}, C_{2mn}, C_{3mn}, H_{1n}, H_{2n}, and H_{3n}:

$$
\begin{aligned}
C_{1mn} = \ & \frac{1-\nu}{DR^2} \ Y'_{mn} \ \frac{\gamma_m}{n^2} \ \{-[n^2 + 4(1-\nu)(1-2\nu) \ n + \gamma_m^2] \ \gamma_m^2 \ I_{n-1}^2 \\
& + 2 \ [-n^4 + 4(1-\nu)(1-2\nu) \ n^3 - \frac{3}{2} \ \gamma_m^2 n^2 + (8\nu^2 - 12\nu + 5) \ n^2 \\
& - 2\nu \ (3-2\nu) \ \gamma_m^2 n - \frac{1}{2} \ \gamma_m^4] \ I_{n+1} + 2[n^4 + 4(2-\nu)(1-2\nu) \ n^3 \\
& + 2 \ \gamma_m^2 n^2 + (24\nu^2 - 36\nu + 11) \ n^2 + 2 \ \gamma_m^2 \ n + \gamma_m^4] \ I_{n-1} \ I_{n+1}\} \\
& + \frac{1-\nu}{DR^3} \ Y_{mn} \ \frac{\gamma_m}{n^2} \ [n^3 - (1-2\nu)n^2 + \gamma_m^2 n - (16\nu^2 - 22\nu +5)n + (1-2\nu)\gamma_m^2] \\
& \gamma_m^2 \ I_{n-1}^2 + [-2n^5 + 2(1-2\nu)n^4 - 3\gamma_m^2 n^3 + 4(2-5\nu + 4\nu^2)n^3 \\
& + (1-10\nu)\gamma_m^2 n^2 + 2(1-8\nu + 8\nu^2)n^2 - \gamma_m^4 n + 3(1-2\nu)\gamma_m^2 n \\
& + (1-2\nu)\gamma_m^4] \ I_{n+1}^2 + 2[-n^5 - (1-2\nu)n^4 - \gamma_m^2 n^3 + (5-18\nu + 18\nu^2)n^3 \\
& + (7-32\nu + 24\nu^2)n^2 - 4(1-\nu)\gamma_m^2 n^2 + (1-8\nu + 8\nu^2)\gamma_m^2 n - (1-2\nu)\gamma_m^4] \\
& I_{n-1} \ I_{n+1}\}
\end{aligned}
$$

$$+ \frac{1-\nu}{DR^3} X_{mn} \frac{\gamma_m}{n^2} \{[(8\nu^2 - 12\nu + 1)n^2 + 4(1-\nu)(1-2\nu)n + \gamma_m^2] \gamma_m^2 I_{n-1}^2$$

$$+ [16\nu(1-\nu)n^4 - 4(1-\nu)(1-4\nu)n^3 + (1+4\nu - 8\nu^2)\gamma_m^2 n^2 - 4(1-\nu)n^2$$

$$+ 8\nu(1-\nu)\gamma_m^2 n + \gamma_m^2] I_{n+1}^2 + [-4(1-8\nu + 4\nu^2)n^4 - 12(1-\nu)(1-4\nu)$$

$$n^3 + 2(3-4\nu)\gamma_m^2 n^2 - 4(1-\nu)n^2 - 4(1-\nu)\gamma_m^2 n - 2\gamma_m^4] I_{n-1} I_{n+1}\}$$

$$+ \frac{1-\nu}{DR^2} X'_{mn} \frac{\gamma_m}{n^2} \{-[n^2 + 4(1-\nu)(1-2\nu)n + \gamma_m^2] \gamma_m^2 I_{n-1}^2$$

$$+ [4(1-\nu)n^3 - \gamma_m^2 n^2 + (1-\nu)n^2 - 8\nu(1-\nu)\gamma_m^2 n - \gamma_m^4] I_{n+1}^2$$

$$+ [4n^4 + 12(1-\nu)n^3 + 6\gamma_m^2 n^2 + 4(1-\nu)n^2 + 4(1-\nu)\gamma_m^2 n + 2\gamma_m^2]$$

$$I_{n-1} I_{n+1}\}$$

$$+ \frac{1-\nu}{DR^4} T_{mn} \frac{\gamma_m}{n} \{n^3 - 2(1-2\nu)n + \gamma_m^2]\gamma_m^2 I_{n-1}^2$$

$$+ [-2n^4 - 3\gamma_m^2 n^2 + 2n^2 - 2(1+2\nu)\gamma_m^2 n - \gamma_m^4] I_{n+1}^2$$

$$+ 2n[-n^3 + (1-\gamma_m^2)n - 2\gamma_m^2] I_{n-1} I_{n+1}\}$$

$$+ \frac{1-\nu}{DR^3} T'_{mn} \frac{\gamma_m}{n^2} \{[-n^2 + 2(1-2\nu)n - \gamma_m^2]\gamma_m^2 I_{n-1}^2 + [-2n^4$$

$$- 3\gamma_m^2 n^2 + 2n^2 - 2(1+2\nu)\gamma_m^2 n - \gamma_m^4] I_{n+1}^2 + 2[n^4 + (2\gamma_m^2 - 1)n^2$$

$$+ 4\nu\gamma_m^2 n + \gamma_m^4] I_{n-1} I_{n+1}\}$$

$$C_{2mn} = \frac{1-\nu}{DR^2} \; Y'_{mn} \; \frac{1}{n^2} \; \{[2n^4 + 8(1-\nu)(1-2\nu)n^3 + 3\gamma_m^2 n^2 - 2(5-12\nu + 8\nu^2)n^2$$

$$+ 4\nu(2\nu-3)\gamma_m^2 n + \gamma_m^4] \; I_{n-1}^2 + [n^2 - 4(1-\nu)(1-2\nu)n + \gamma_m^2]\gamma_m^2$$

$$I_{n+1}^2 + 2[-n^4 + 4(2-\nu)(1-2\nu)n^3 - 2\gamma_m^2 n^2 - (11-36\nu + 24\nu^2)n^2$$

$$+ 2\gamma_m^2 n - \gamma_m^4] \; I_{n-1} \; I_{n+1}\}$$

$$+ \frac{1-\nu}{DR^3} \; Y_{mn} \; \frac{\gamma_m}{n^2} \; \{[-2n^5 -2(1-2\nu)n^4 - 3\gamma_m^2 n^3 + 2(1-2\nu)(3-4\nu)n^3$$

$$- (1-10\nu)\gamma_m^2 n^2 - 2(1-8\nu + 8\nu^2)n^2 + 3(1-2\nu)\gamma_m^2 n - \gamma_m^4 n$$

$$- (1-2\nu)\gamma_m^4] \; I_{n-1}^2 + [n^3 + (1-2\nu)n^2 - (5-22\nu + 16\nu^2)n$$

$$- (1-2\nu)\gamma_m^2]\gamma_m^2 \; I_{n+1}^2 + 2[-n^5 + (1-2\nu)n^4 - \gamma_m^2 n^3 + (5$$

$$- 18\nu + 8\nu^2)n^3 + 4(1-\nu)\gamma_m^2 n^2 - (7-32\nu + 24\nu^2)n^2 + (1-8\nu + 8\nu^2)$$

$$\gamma_m^2 n + (1-2\nu)\gamma_m^4] \; I_{n-1} \; I_{n+1}\}$$

$$+ \frac{1-\nu}{DR^2} \; X'_{mn} \; \frac{\gamma_m}{n^2} \; \{[-4(1-\nu)n^3 - \gamma_m^2 n^2 + 4(1-\nu)n^2 + 8\nu(1-\nu)\gamma_m^2 n$$

$$- \gamma_m^4] \; I_{n-1}^2 + [-n^2 + 4(1-\nu)(1-2\nu)n - \gamma_m^2]\gamma_m^2 \; I_{n+1}^2 + [4n^4$$

$$- 12(1-\nu)n^3 + 6\gamma_m^2 n^2 + 4(1-\nu)n^2 - 4(1-\nu)\gamma_m^2 n + 2\gamma_m^4] \; I_{n-1} \; I_{n+1}\}$$

$$+ \frac{1-\nu}{DR^3} \; X_{mn} \; \frac{\gamma_m}{n^2} \; \{[16\nu(1-\nu)n^4 + 4(1-\nu)(1-4\nu)n^3 + (1+4\nu - 8\nu^2)\gamma_m^2 n^2$$

$$- 4(1-\nu)n^2 - 8\nu(1-\nu)\gamma_m^2 n + \gamma_m^4] \; I_{n-1}^2 + [2(1-12\nu + 8\nu^2)n^2 - 4(1-\nu)$$

$$(1-2\nu)n + \gamma_m^2]\gamma_m^2 \; I_{n+1}^2 + [-4(1-8\nu + 4\nu^2)n^4 + 12(1-\nu)(1-4\nu)n^3$$

$$- 2(3-4\nu)\gamma_m^2 n^2 - 4(1-\nu)n^2 + 4(1-\nu)\gamma_m^2 n - 2\gamma_m^4] \; I_{n-1} \; I_{n+1}\}$$

$$+ \frac{1-\nu}{DR^3} T'_{mn} \frac{1}{n^2} \{[2n^4 + (3\gamma_m^2 - 2)n^2 - 2(1+2\nu)\gamma_m^2 n + \gamma_m^4] I_{n-1}^2$$

$$+ [n^2 + 2(1-2\nu)n + \gamma_m^2]\gamma_m^2 I_{n+1}^2 + 2[-n^4 + (1-2\gamma_m^2)n^2$$

$$+ 4\nu\gamma_m^2 n - \gamma_m^4] I_{n-1} I_{n+1}\}$$

$$+ \frac{1-\nu}{DR^4} T_{mn} \frac{1}{n} \{[-2n^4 + (2-3\gamma_m^2)n^2 + 2(1+2\nu)\gamma_m^2 n - \gamma_m^4] I_{n-1}^2$$

$$+ [n^2 + 2(1-2\nu)n + \gamma_m^2]\gamma_m^2 I_{n+1}^2 + 2[-n^4 + (1-\gamma_m^2)n^2 + 2 \gamma_m^2 n]$$

$$I_{n-1} I_{n+1}\}$$

$$C_{3mn} = \frac{1-\nu}{DR} Y'_{mn} \frac{1}{n} \{2[n^2 - 8\nu(1-\nu)n + \gamma_m^2 - 2(1-\nu)(3-12\nu + 8\nu^2)]\gamma_m^2$$

$$I_{n-1}^2 + 2[-n^2 - 8\nu(1-\nu)n - \gamma_m^2 + 2(1-\nu)(3-12\nu + 8\nu^2)]\gamma_m^2 I_{n+1}^2$$

$$+ 16n [-(1-6\nu + 4\nu^2)n^2 - (1-2\nu + 2\nu^2) \gamma_m^2 + 2(3-12\nu + 8\nu^2)(1-\nu)]$$

$$I_{n-1} I_{n+1} \}$$

$$+ \frac{1-\nu}{DR^2} Y_{mn} \frac{1}{n^2} \{2[-2n^4 + (3-4\nu)n^3 - 3 \gamma_m^2 n^2 + 4(1-\nu)(3-10\nu + 4\nu^2)n^2$$

$$+ 3\gamma_m^2 n - 6(1-\nu)(3-12\nu + 8\nu^2)n - \gamma_m^4 + 2(1-\nu)(3-12\nu + 8\nu^2)]\gamma_m^2$$

$$I_{n-1}^2 + 2[-2n^4 - (3-4\nu)n^3 - 3\gamma_m^2 n^2 + 4(1-\nu)(3-10\nu + 4\nu^2)n^2$$

$$- 3\gamma_m^2 n + 6(1-\nu)(3-12\nu + 8\nu^2)n - \gamma_m^4 + 2(1-\nu)(3-12\nu + 8\nu^2)]\gamma_m^2$$

$$I_{n+1}^2 + 4[2n^6 + 4\gamma_m^2 n^4 - 4(4-13\nu + 8\nu^2)n^4 + 3\gamma_m^4 n^2 + 4(-4+13\nu$$

$$- 14\nu^2 + 4\nu^3)\gamma_m^2 n^2 + 8(1-\nu)(3-12\nu + 8\nu^2)n^2 + \gamma_m^6 - 2(1-\nu)(3-12\nu$$

$$+ 8\nu^2)\gamma_m^4] I_{n-1} I_{n+1} \}$$

$$+ 2 \frac{1-\nu}{DR} X'_{mn} \frac{1}{n} \{[n^2 - 8\nu(1-\nu)n + \gamma_m^2 - 2(1-\nu)(3-12\nu + 8\nu^2)]\gamma_m^2 I_{n-1}^2$$

$$+ [n^2 + 8\nu(1-\nu)n + \gamma_m^2 - 2(1-\nu)(3-12\nu + 8\nu^2)]\gamma_m^2 I_{n+1}^2$$

$$+ 2[-2n^4 - 3\gamma_m^2 n^2 + 4(1-\nu)(3-4\nu)n^2 - \gamma_m^4 + 2(1-\nu)(3-12\nu + 8\nu^2)\gamma_m^2]$$

$$I_{n-1} I_{n+1}\}$$

$$+ 2\frac{1-\nu}{DR^2} X_{mn} \frac{1}{n} \{[(-1+20\nu - 16\nu^2)n^2 - 8\nu(1-\nu)(3-2\nu)n - (1-8\nu + 8\nu^2)$$

$$- \gamma_m^2 + 2(1-\nu)(3-12\nu + 8\nu^2)]\gamma_m^2 I_{n-1}^2 + [(-1+20\nu - 16\nu^2)n^2 + 8\nu(1-\nu)(3$$

$$-2\nu)n + (1-8\nu + 8\nu^2)\gamma_m^2 + 2(1-\nu)(3-12\nu + 8\nu^2)]\gamma_m^2 I_{n+1}^2 + 2[2(1-12\nu$$

$$+ 8\nu^2)n^4 + (3-20\nu + 16\nu^2)\gamma_m^2 n^2 - 4(1-\nu)(3-20\nu + 16\nu^2)n^2 + (1-8\nu$$

$$+ 8\nu^2)\gamma_m^4 - 2(1-\nu)(3-12\nu + 8\nu^2)\gamma_m^2] I_{n-1} I_{n+1}\}$$

$$+ \frac{1-\nu}{DR} T'_{mn} \frac{1}{n^2} \{2[n^3 - 2(5-10\nu + 4\nu^2)n^2 + \gamma_m^2 n + 2(1-\nu)(5-8\nu)n - 4(1$$

$$-\nu)(1-2\nu)\gamma_m^2]\gamma_m^2 I_{n-1}^2 + 2[-n^3 - 2(5-10\nu + 4\nu^2)n^2 - \gamma_m^2 n$$

$$- 2(1-\nu)(5-8\nu)n - 4(1-\nu)(1-2\nu)\gamma_m^2]\gamma_m^2 I_{n+1}^2 + 8[4(1-\nu)n^4 + (3-10\nu$$

$$+ 4\nu^2)\gamma_m^2 n^2 - 4(1-\nu)n^2 + 2(1-\nu)(1-2\nu)\gamma_m^4] I_{n-1} I_{n+1}\}$$

$$+ 2 \frac{1-\nu}{DR^2} T_{mn} \frac{1}{n^2} \{[-2n^4 + 2(2-3\nu)n^3 - 3\gamma_m^2 n^2 - (3-12 + 8\nu^2)n^2 + 2(2$$

$$-\nu)\gamma_m^2 n - \gamma_m^4]\gamma_m^2 I_{n-1}^2 + [-2n^4 - 2(2-3\nu)n^3 - 3\gamma_m^2 n^2 + (3-12\nu$$

$$+ 8\nu^2)n^2 - 2(2-\nu)\gamma_m^2 n - \gamma_m^4]\gamma_m^2 I_{n+1}^2 + 2[2n^6 + (4\gamma_m^2 - 2)n^4 + 3\gamma_m^4 n^2$$

$$- (5+4\nu - 8\nu^2)\gamma_m^2 n^2 + \gamma_m^6] I_{n-1} I_{n+1}\}$$

$$H_{1n} = \frac{2}{D_o} R^{2n-5} (1-\nu)n \{[-n^2 - 4(1-\nu)(1-2\nu)n + 5-12\nu + 8\nu^2]R^2 Y'_{on}$$

$$+ [n^3 + (1-2\nu)n^2 - (1-2\nu)(3-4\nu)n + 1 - 8\nu + 8\nu^2]RY_{on} + 2(1-\nu)(n$$

$$-1)R^2 X'_{on} + 2(1-\nu)[-4\nu n^2 - (1-4\nu)n + 1]RX_{on} - (n^2-1)RT'_{on}$$

$$+ n(n^2-1) T_{on}\}$$

$$H_{2n} = \frac{2(1-\nu)}{D_o} R^{2n-3}n \{[-n^2 - 2(1-2\nu + 4\nu^2)n + 3-12\nu + 8\nu^2]R^2 Y'_{on}$$

$$+ [n^3 - (1-6\nu)n^2 - (7-30\nu + 24\nu^2)n - 3+12\nu - 8\nu^2]RY_{on} - 2[(2$$

$$- 9\nu + 8\nu^2)n - (1-\nu)(3-8\nu)]R^2 X'_{on} + 2[-4\nu(1-\nu)n^2 + (2-\nu)(1-4\nu)n$$

$$+ (1\nu)(3-8\nu)]RX_{on} + [-n^2 + 2(1-4\nu)n + (3-8\nu)] RT'_{on} + [n^2$$

$$- 2(1-4\nu)n - (3-8\nu)]n T_{on}\}$$

$$H_{3n} = \frac{2(1-\nu)}{D_o} R^{2n-3} \{[n^3 - (1-4\nu)n^2 + 2(1-\nu)(-3+8\nu - 8\nu^2)n + 2(1-$$

$$\nu)(3-12\nu + 8\nu^2)]R^2 Y'_{on} + [-n^4 + (1-4\nu)n^3 + (1-2\nu)(7-16\nu + 8\nu^2)n^2$$

$$- 2(1-\nu)(3-16\nu + 16\nu^2)n - 2(1-\nu)(3-12\nu + 8\nu^3)]RY_{on} + [(1-8\nu$$

$$+ 8\nu^2)n^2 + 8\nu(1-\nu)(1-2\nu)n + 2(1-\nu)(-3+12\nu - 8\nu^2)]R^2 X'_{on}$$

$$+ [8\nu(1-\nu)n^3 + (-1-4\nu + 24\nu^2 - 16\nu^3)n^2 - 8\nu(1-\nu)n + 2(1-\nu)$$

$$(3-12\nu + 8\nu^2)]RX_{on} + [n^3 - (5-16\nu + 8\nu^2)n^2 - 2\nu(3-4\nu)n$$

$$+ 2(1-\nu)(3-8\nu)]RT'_{on} + [-n^4 + 2(1-3\nu)n^3 + 2\nu(3-4\nu)n^2 + (-3$$

$$+ 12\nu - 8\nu^2)]T_{on}\} \tag{24}$$

where

$$D = \frac{(1-\nu)\gamma_m}{R^3 n^3} \{2\gamma_m^2 n [(1-\nu)(3-4\nu)n^2 - \nu(5-4\nu)\gamma_m^2](I_{n-1}^3 + I_{n+1}^3)$$

$$+ \gamma_m^2 [n^4 + (2\gamma_m^2 - 7+14\nu - 8\nu^2)n^2 + \gamma_m^4](I_{n-1}^3 - I_{n+1}^3) + 2n [-8(1$$

$$-\nu)n^4 + (1+7\nu - 4\nu^2)\gamma_m^2 n^2 + 8(1-\nu)n^2 + \nu(5-4\nu)\gamma_m^4] \, I_{n-1} \, I_{n+1}$$

$$(I_{n-1} + I_{n+1}) + [-4n^6 + (4-11\gamma_m^2)n^4 + (-10\gamma_m^2 - 3+46\nu - 40\nu^2)\gamma_m^2 n^2$$

$$- 3\gamma_m^6] I_{n-1} \, I_{n+1} \, (I_{n-1} - I_{n+1})\}$$

$$D_o = 2R^{3n-3} \, (1-\nu)(1-2\nu)(3-4\nu)(n^2-1)n \tag{25}$$

The symbols I_{n-1}, I_n and I_{n+1} appearing here represent modified Bessel functions of the first kind of argument $\gamma_m \equiv \lambda_m R$.

The particular solutions constituting parts of eqs. (21) and (22) have been found by applying the method of variation of the constants:

$$\bar{\bar{\Psi}}_{rp}(r,n,m) = -\frac{1}{2}Z_{1mn}(r) \, I_{n+1}(\lambda_m r) + \frac{1}{2}Z_{2mn}(r) \, K_{n+1}(\lambda_m r)$$

$$- \frac{1}{2}Z_{3mn}(r) \, I_{n-1}(\lambda_m r) + \frac{1}{2}Z_{4mn}(r) \, K_{n-1}(\lambda_m r)$$

$$\bar{\bar{\Psi}}_{\theta p}(r,n,m) = \frac{1}{2} Z_{1mn}(r) \, I_{n+1}(\lambda_m r) - \frac{1}{2}Z_{2mn}(r) \, K_{n+1}(\lambda_m r)$$

$$- \frac{1}{2}Z_{3mn}(r) \, I_{n-1}(\lambda_m r) + \frac{1}{2}Z_{4mn}(r) \, K_{n-1}(\lambda_m r)$$

$$\bar{\bar{\Phi}}_p(r,n,m) = Z_{5mn}(r) \, I_n(\lambda_m r) - Z_{6mn}(r) \, K_n(\lambda_m r)$$

$$\bar{\bar{\Psi}}_{rp}(r,n,0) = \frac{1}{4(n+1)} \, [r^{n+1} \, Z_{1on}(r) - r^{-(n+1)} \, Z_{2on}(r)]$$

$$+ \frac{1}{4(n-1)} \, [r^{n-1} \, Z_{3on}(r) - r^{-(n-1)} \, Z_{4on}(r)]$$

$$\bar{\bar{\Psi}}_{\theta p}(r,n,0) = \frac{1}{4(n+1)} \, [-r^{n+1} \, Z_{1on}(r) + r^{-(n+1)} \, Z_{2on}(r)]$$

$$+ \frac{1}{4(n-1)} \, [r^{n-1} \, Z_{3on}(r) - r^{-(n-1)} \, Z_{4on}(r)]$$

$$\bar{\bar{\Phi}}_p(r,n,0) = \frac{1}{2n} \, [r^n \, Z_{50n}(r) - r^{-n} \, Z_{60n}(r)] \tag{26}$$

where

$$Z_{1mn}(r) = \int_0^r [G_{1n}(\rho) - (-1)^m G_{2n}(\rho) - G_{3n}(\rho) + (-1)^m G_{4n}(\rho)]$$

$$[K_{n+1}(\lambda_m\rho)/M_{n+1}(\lambda_m\rho)]d\rho$$

$$Z_{2mn}(r) = \int_0^r [G_{1n}(\rho) - (-1)^m G_{2n}(\rho) - G_{3n}(\rho) + (-1)^m G_{4n}(\rho)]$$

$$[I_{n+1}(\lambda_m\rho)/M_{n+1}(\lambda_m\rho)]d\rho$$

$$Z_{3mn}(r) = \int_0^r [G_{1n}(\rho) - (-1)^m G_{2n}(\rho) + G_{3n}(\rho) - (-1)^m G_{4n}(\rho)]$$

$$[K_{n-1}(\lambda_m\rho)/M_{n-1}(\lambda_m\rho)]d\rho$$

$$Z_{4mn}(r) = \int_0^r [G_{1n}(\rho) - (-1)^m G_{2n}(\rho) + G_{3n}(\rho) - (-1)^m G_{4n}(\rho)]$$

$$[I_{n-1}(\lambda_m\rho)/M_{n-1}(\lambda_m\rho)]d\rho$$

$$Z_{1on}(r) = \int_0^r [G_{1n}(\rho) - G_{2n}(\rho) - G_{3n}(\rho) + G_{4n}(\rho)]\rho^{-n} \, d\rho$$

$$Z_{2on}(r) = \int_0^r [G_{1n}(\rho) - G_{2n}(\rho) - G_{3n}(\rho) + G_{4n}(\rho)]\rho^{n+2} \, d\rho$$

$$Z_{3on}(r) = \int_0^r [G_{1n}(\rho) - G_{2n}(\rho) + G_{3n}(\rho) - G_{4n}(\rho)]\rho^{-n+1} \, d\rho$$

$$Z_{4on}(r) = \int_0^r [G_{1n}(\rho) - G_{2n}(\rho) + G_{3n}(\rho) - G_{4n}(\rho)]\rho^{n} \, d\rho$$

$$Z_{5mn}(r) = \int_0^r [G_{1n}(\rho) - (-1)^m G_{2n}(\rho)][\rho K_n(\lambda_m\rho)/M_n(\lambda_m\rho)]d\rho$$

$$Z_{6mn}(r) = \int_0^r [G_{1n}(\rho) - (-1)^m G_{2n}(\rho)][\rho I_n(\lambda_m\rho)/M_n(\lambda_m\rho)]d\rho$$

$$Z_{5on}(r) = \int_0^r [G_{2n}(\rho) - G_{1n}(\rho)]\rho^{-n+2} \, d\rho$$

$$Z_{6on}(r) = \int_o^r [G_{2n}(\rho) - G_{1n}(o)]\rho^{n+2} \, d\rho \qquad (27)$$

and where

$$M_n(\lambda_m\rho) \equiv K'_n(\lambda_m\rho) \, I_n(\lambda_m\rho) - K_n(\lambda_m\rho) \, I'_n(\lambda_m\rho) \qquad (28)$$

As it is seen there are 4 unknown functions to be determined: $G_{1n}(\rho)$, ..., $G_{4n}(\rho)$.

To this end one has to substitute the expressions (21) and (22) to the inversion formulas for the Fourier transformation with respect to the variable z. Once this is done the conditions at the flat ends eqs. 13.1, 13.2, 14.1 and 14.2 are to be applied (notice that condition 13.3 is satisfied automatically) leading to a system of Fredholm's integral equations of the first kind with respect to aforementioned functions. Solution of this system will provide necessary information for the evaluation of stresses.

References

[1] Achenbach, J.D., Wave Propagation in Elastic Solids, North-Holland Publ. Co., 1973.

[2] Sokolnikoff, I.S., Mathematical Theory of Elasticity, McGraw-Hill, 1956.

APPENDIX 2: Controlled Impact of a Finite Elastic Rod Upon an Isotropic,
Elastic Half-space.

1. Introduction

The present paper is concerned with the state of stress in a finite elastic rod striking a stationary, isotropic, elastic half-space. The motion of the far end of the rod is controlled in such a way that the depth of the indentation is within the limits of linear elasticity. In order to avoid the difficulty resulting from the fact that the normal displacement of an elastic half-space is singular at the point of application of the concentrated force it is assumed that the reaction of the rod is uniformly distributed over the circular area corresponding to the rod's cross-section.

2. The Solution for the rod

Let u_1 denote axial displacement of the rod, x - spatial coordinate measured along its axis from the far end, and E, ρ - Young modulus and mass per unit volume of the rod's material respectively. The equation of motion of the rod takes the following form:

$$\frac{\partial^2 u_1}{\partial t^2} = \frac{E}{\rho} , \ 0 \le x \le L, \ t > 0 \tag{1}$$

Let the function f(t) describing controlled motion of the far end of the rod be defined in such a way to assure that the displacement be zero at t = 0

$$u_1(0,t) = f(t), \ f(0) = 0, \ t > 0 \tag{2}$$

At the striking end of the rod the following continuity conditions must be satisfied:

$$u_1(L,t) = w(0,0,t) \equiv w(t), \ 0 \le t \le t_1 \tag{3}$$

$$E \frac{\partial u_1(L,t)}{\partial x} = (\lambda_s + 2\mu_s) \frac{\partial w(0,0,t)}{\partial z} + \lambda_s \frac{\partial u(0,0,t)}{\partial r} , \ 0 \le t \le t_1 \tag{4}$$

where

$$w(0,0,t) = \lim w(r,z,t)$$

$$u(0,0,t) = \lim u(r,z,t) \text{ for } r, z \to 0$$

are the vertical and radial components of the displacement of the half-space at the impact point referred to polar coordinate system r, z. The axes z and x are collinear; t_1 denotes the separation time and the subscript s describes the coefficients related to half-space. The initial conditions for the rod are:

$$u_1(x,0) = 0, \quad \frac{\partial u_1(x,0)}{\partial t} = V = \text{const.} \quad 0 \leq x \leq L \tag{5}$$

while for the half-space they are

$$u(r,z,0) = w(r,z,0) = \frac{\partial u(r,z,0)}{\partial t} = \frac{\partial w(r,z,0)}{\partial t} = 0 \tag{6}$$

The elimination of the variable x from eq. 1 is achieved by applying finite Fourier sine transformation

$$S\{u_1\} \equiv u_m(t) = \int_0^L u_1(x,t)\sin \alpha_m x \, dx \qquad m = 1, 2, \ldots \tag{7}$$

where $\alpha_m = m\pi/L$.

The transformed eq. (1) takes the following form

$$\frac{d^2 u_m(t)}{dt^2} + \frac{E}{\rho} \alpha_m^2 u_m(t) = \frac{E}{\rho} \alpha_m [f(t) - (-1)^m w(t)] \tag{8}$$

$$0 \leq t \leq t_1$$

where the boundary conditions (2) and (3) have been taken into account.

Solution of the eq. (8) with consideration of the transformed conditions (5) becomes:

$$u_m(t) = \frac{1-(-1)^m}{\alpha_m^2} V \sqrt{\rho/E} = \sqrt{E/\rho} \int_0^t [(f/\tau) - (-1)^m w(\tau)]$$

$$\sin \varepsilon_m(t-\tau)d\tau \qquad\qquad 0 \leq t \leq t \tag{9}$$

where

$$\varepsilon_m = \alpha_m \sqrt{E/\rho}.$$

Applying the inversion formula one obtains from (9)

$$u_1(x,t) = (2VL/\pi^2) \sqrt{\rho/E} \sum_{m=1}^{\infty} \frac{1-(-1)^m}{m^2} \sin \varepsilon_m t \sin \alpha_m x$$

$$+ (2/L) \sqrt{E/\rho} \int_0^t \{f(\tau) \sum_{m=1}^{\infty} \sin \varepsilon_m(t-\tau) \sin \alpha_m x$$

$$- w(\tau) \sum_{m=1}^{\infty} (-1)^m \sin \varepsilon_m(t-\tau) \sin \alpha_m x\} \, d\tau \qquad 0 \le t \le t_1 \qquad (10)$$

Eq. (10) can be finally put in the form

$$u_1(x,t) = (2VL/\pi^2)A(x,t) \sqrt{\rho/E} + U_1(x,t) - U_2(x,t) \qquad t \le t_1 \qquad (11)$$

where for $\bar{t} \le L/2$ $(\bar{t} = t\sqrt{E/\rho})$

$$A(x,t) = \sum_{m=1}^{\infty} \frac{1-(-1)^m}{m^2} \sin \varepsilon_m t \sin \alpha_m x = \{ \begin{matrix} \pi^2 x/2L & , & x \le \bar{t} \\ \pi^2 \bar{t}/2L & , & \bar{t} \le x \le L - \bar{t} \\ \pi^2(L-x)/2L, & L-\bar{t} \le x \le L \end{matrix} \qquad (12)$$

and similar results can be obtained for $\bar{t} > L/2$.

Also using the result

$$\sum_{m=1}^{\infty} \sin m \bar{\tau} \sin m\pi x/L = \frac{L}{2} \delta(x-\frac{L}{\pi} \bar{\tau}+LM) \text{ for } M = 0,2,4,\ldots$$

and similarly for $M=1,3,5,\ldots$, where δ is Dirac's delta, and also applying the sifting property of δ it was found that:

$$U_1(x,t) = f(t - x \sqrt{\rho/E}) - f[t-(2L-x) \sqrt{\rho/E}]$$

$$+ f[t-(2L+x) \sqrt{\rho/E}] - \ldots+(-1)^M f \{t- [(-1)^M x$$

$$+ ML + \frac{1-(-1)^M}{2} L] \sqrt{\rho/E} \} \qquad t \le t_1 \qquad (13)$$

$$U_2(x,t) = -w[t-(L-x) \sqrt{\rho/E}] + w[t-(L+x) \sqrt{\rho/E}]$$

$$- w[t-(3L-x) \sqrt{\rho/E}] +\ldots+(-1)^{M+1} w\{t- [$$

$$(-1)^{M+1} x + (M+ \frac{1+(-1)^M}{2})L]\sqrt{\rho/E} \} \qquad t \le t_1 \qquad (14)$$

The displacement (11) depends on the still unknown function $w(t)$.

3. Solution for elastic half-space

The satisfaction of the boundary conditions (3) and (4) demands that the

vertical displacement $w(t) \equiv w(0,0,t)$ of the half-space subjected to time varying pressure from the rod be determined. Since this pressure is concentrated at a point it becomes therefore necessary to apply SAITO and CHONAN's [1] approximated procedure. Hence it is assumed that the rod's pressure is distributed uniformly over the disc equal to the cross-section of the rod. The contact between the rod and the half-space is maintained -- as originally assumed -- only at the center of the disc.

As an auxiliary problem one has to determine vertical deflection $w_1(r,z,t)$ of the half-space loaded uniformly over a circular disc by a suddenly applied constant unit load. The solution of this problem has been obtained by EASON [2] and it takes the following form for $r = z = 0$:

$$\frac{2\pi\mu}{a} w_1(0,0,\tau) = \frac{\pi\beta^2}{\beta^2-1} + \frac{\beta^2\pi}{G}\frac{\sqrt{1-\alpha^2}}{a}\frac{\sqrt{a^2-\alpha^2\tau^2}}{a}$$

$$-\frac{\beta^2}{a}\int_1^{a/\tau}\frac{y\sqrt{(y^2-1)(a^2-y^2\tau^2)}\,dy}{(1-\frac{1}{2}\beta^2y^2)^2+\sqrt{(y^2-1)(\beta^2y^2-1)}}$$

$$-\frac{\beta^2}{a}\int_{1/\beta}^1\frac{y(1-y^2)\sqrt{(\beta^2y^2-1)(a^2-y^2\tau^2)}\,dy}{(1-\frac{1}{2}\beta^2y^2)^4+(1-y^2)(\beta^2y^2-1)} \qquad \text{for } 0 \leq \tau \leq a \qquad (15)$$

and similar expressions valid for $a \leq \tau \leq \beta a$ etc.

The following abbreviations have been used here

$$\beta^2 = (\lambda_s + 2\mu_s)/\mu_s, \quad G = 2\beta^2(1-\frac{1}{2}\beta^2\alpha^2) - \sqrt{\frac{1-\beta^2\alpha^2}{1-\alpha^2}}$$

$$-\beta^2\sqrt{\frac{1-\alpha^2}{1-\beta^2\alpha^2}}, \quad \tau = c_1 t, \quad c_1 = \sqrt{(\lambda_s+2\mu_s)/\rho_s} \qquad (16)$$

where α is the coefficient of the root $s = i\,\alpha\xi$ of the following equation

$$(\xi^2 + \frac{1}{2}\beta^2 s^2)^2 - \xi^2\sqrt{(\xi^2+s^2)(\xi^2+\beta^2 s^2)} = 0 \qquad (17)$$

In order to obtain the result valid for a load $h(t)$ varying arbitrarily in time one has to use the following relationship

$$X(t) = \int_0^t h(\xi) \, X_1'(t-\xi) d\xi = \int_0^t h(t-\xi) X_1' \, (\xi) \, d\xi \qquad (18)$$

relating the response $X(t)$ to arbitrary excitation $h(t)$ to the response $X_1(t)$ to HEAVISIDE type of excitation.

The resultant force at the striking end of the rod is obtained from

$$q(t) = -E \frac{\partial u_1(L,t)}{\partial x} \pi a^2 \qquad t \le t_1 \qquad (19)$$

where eq. 11 should be substituted for $u_1(L,t)$.

4. The conditional equation

Using eq. (18) the following VOLTERRA's integro-differential equation with respect to the unknown function $w(t)$ is obtained

$$w(t) = \int_0^t q(t-\xi) w_1' \, (0,0,\xi) \, d\xi \qquad (20)$$

where $q(t)$ depends on $w(t)$ through eqs. (19), (11) and (14). Integrating eq. (20) by parts one gets the formula

$$w(t) = \int_0^t w_1(0,0,t-\xi) \frac{dq(\xi)}{d\xi} \, d\xi \qquad (21)$$

The LAPLACE transform of (21) takes the form

$$\overline{w} = p \, \overline{w}_1 \overline{q} \qquad (22)$$

where p is the parameter of the transformation and $\overline{w}$ is the transform of $w(t)$ etc.

After numerous rearrangements the following explicit equation for $\overline{w}$ results from eq. (22):

$$\overline{w} \, \{1 + \sqrt{E\rho} \, \pi^2 a^2 p^2 \overline{w}_1 \, [1 + 2e^{-2pb} + 2e^{-4pb} + \ldots] \}$$
$$= - p\overline{w}_1 \pi a^2 \sqrt{E\rho} \, \{\frac{V}{p} \, [-1 + 2e^{-pb} - 2e^{-2pb} + \ldots]$$
$$+ 2p\overline{T} \, [e^{-pb} + e^{-3pb} + \ldots]\} \qquad (23)$$

where $b = L \sqrt{\rho/E}$.

In order to obtain $w(t)$ what is necessary for the analysis, through eqs. (11) and (14), of the history of displacement and of stress in the rod, one must invert $\bar{w}$ resulting from eq. (23). This can be achieved by using continued fraction representation as done by AKIN and COUNTS in [3].

REFERENCES

1. Saito, H., Chonan, S. Forced longitudinal vibration of an elastic circular rod on an elastic half-space. J. AC. SOC. AMER. 59, 4, 1976, 861-865.

2. Eason, G. The Displacements Produced in an Elastic Half-space by a Suddenly Applied Surface Force. J. INST. MATHS. APPLICS. 2, 1966, 299-326.

3. Akin, J.E., Counts, J. The Application of Continued Fractions to Wave Propagation in a Semi-Infinite Elastic Cylindrical Membrane. J. APPL. MECH., 36, 3, 1969, 420-424.

This report documents research conducted under AFOSR Grant 77-3087 conducted during the period July 8, 1977 through July 7, 1978.

Stephen L. Rice
Principal Investigator

Roman Solecki
Co-Principal Investigator

INSTITUTE OF MATERIALS SCIENCE

The Institute of Materials Science was established at The University of Connecticut in 1966 in order to promote the various fields of materials science. To this end, the State of Connecticut appropriated $5,000,000 to set up new laboratory facilities, including approximately $2,150,000 for scientific equipment. In addition, an annual budget of several hundred thousand dollars is provided by the State Legislature to support faculty and graduate student salaries, supplies and *commodities, and supporting* facilities such as various shops, technicians, secretaries, etc.

IMS fosters interdisciplinary graduate programs on the Storrs campus and at present is supporting five such programs in Alloy Physics, Biomaterials, Crystal Science, Metallurgy, and Polymer Science. These programs are directed toward training graduate students while advancing the frontiers of our knowledge in technically important areas.